



Review

# A State-of-the-Art Review on CMOS Radio Frequency Power Amplifiers for Wireless Communication Systems

Sofiyah Sal Hamid <sup>1</sup>, Selvakumar Mariappan <sup>1,\*</sup> , Jagadheswaran Rajendran <sup>1</sup> , Arvind Singh Rawat <sup>2</sup> , Nuha A. Rhaffor <sup>1</sup> , Narendra Kumar <sup>3</sup>, Arokia Nathan <sup>4</sup> and Binboga S. Yarman <sup>5</sup>

<sup>1</sup> Collaborative Microelectronics Design Excellence Centre (CEDEC), Universiti Sains Malaysia, Bayan Lepas 11900, Malaysia; sofiyah@usm.my (S.S.H.); jaga.rajendran@usm.my (J.R.); nuha@usm.my (N.A.R.)

<sup>2</sup> School of Computing, DIT University, Dehradun 248009, Uttarakhand, India; arvindsrawat@ieee.org

<sup>3</sup> Department of Electrical Engineering, Faculty of Engineering, University of Malaya, Kuala Lumpur 50603, Malaysia; narendra.k@um.edu.my

<sup>4</sup> Darwin College, Cambridge University, Cambridge CB3 9EU, UK; an299@cam.ac.uk

<sup>5</sup> Department of Electrical and Electronics Engineering, Istanbul University, 34320 Istanbul, Turkey; sbyarman@gmail.com

\* Correspondence: selva\_kumar@usm.my

**Abstract:** Wireless communication systems have undergone significant development in recent years, particularly with the transition from fourth generation (4G) to fifth generation (5G). As the number of wireless devices and mobile data usage increase, there is a growing need for enhancements and upgrades to the current wireless communication systems. CMOS transceivers are increasingly being explored to meet the requirements of the latest wireless communication protocols and applications while achieving the goal of system-on-chip (SoC). The radio frequency power amplifier (RFPA) in a CMOS transmitter plays a crucial role in amplifying RF signals and transmitting them from the antenna. This state-of-the-art review paper presents a concise discussion of the performance metrics that are important for designing a CMOS PA, followed by an overview of the trending research on CMOS PA techniques that focuses on efficiency, linearity, and bandwidth enhancement.

**Keywords:** CMOS; radio frequency; power amplifier; wireless communication; efficiency; linearity; bandwidth



**Citation:** Hamid, S.S.; Mariappan, S.; Rajendran, J.; Rawat, A.S.; Rhaffor, N.A.; Kumar, N.; Nathan, A.; Yarman, B.S. A State-of-the-Art Review on CMOS Radio Frequency Power Amplifiers for Wireless

Communication Systems. *Micromachines* **2023**, *14*, 1551. <https://doi.org/10.3390/mi14081551>

Academic Editor: Zhiming Chen

Received: 19 June 2023

Revised: 28 July 2023

Accepted: 29 July 2023

Published: 1 August 2023



**Copyright:** © 2023 by the authors. Licensee MDPI, Basel, Switzerland. This article is an open access article distributed under the terms and conditions of the Creative Commons Attribution (CC BY) license (<https://creativecommons.org/licenses/by/4.0/>).

## 1. Introduction

Wireless communication systems based on radio frequency (RF) technology have become ubiquitous in electronic devices, particularly for mobile applications. As the number of subscribers continues to increase, the demand for RF communication systems also grows. Figure 1 illustrates the trend in mobile subscriptions by technology up to recent times [1]. The power amplifier (PA) block is a crucial component in transceiver design, as it consumes a significant amount of DC power. III-V compound semiconductors such as GaN HEMT, GaAs HBT, Si Bipolar, and SiGe HBT are commonly used to fabricate PAs, as they offer high linear output power and efficiency compared to the silicon CMOS process. However, these PAs are limited in their ability to integrate with CMOS baseband chips, hindering the development of a true single-chip radio or system-on-chip (SoC) [2]. To address this limitation, there was a recent focus on researching CMOS-based RF integrated circuits (RFICs) for wireless mobile applications [3–10]. However, CMOS-based PAs have several disadvantages due to their lower breakdown voltage, their higher substrate loss, and the unavailability of back via holes for the ground connection, which limit the achievable output power and efficiency compared to their III-V counterparts [11–13]. Despite their disadvantages, CMOS-based PAs offer a promising alternative due to their cost-effectiveness and potential for integration with other circuits. Several techniques were developed to improve the efficiency, linearity, and bandwidth performance of CMOS PAs [14–17].

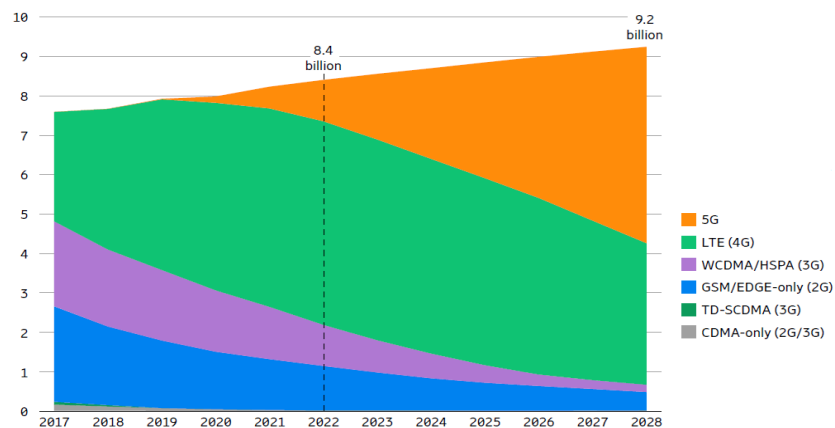


Figure 1. Mobile subscription trend [1].

Efficiency enhancement techniques are usually employed for highly linear PAs that consume more DC power. In contrast, linearity enhancement techniques are commonly employed for switching-based PAs, which have a low conduction angle that contributes to their non-linearity. Efficiency enhancement techniques target the efficiency of linear power amplifiers, while linearization techniques improve the linearity of highly efficient but non-linear power amplifiers [18]. As a result, there is an inevitable trade-off between efficiency and linearity performance in CMOS PAs. Recently, the bandwidth enhancement of CMOS PAs was also widely researched [19].

Wireless communication standards have rapidly expanded in recent years, with different applications utilizing various frequency bands such as L, S, C, UHF, and VHF, which are utilized by applications such as WLAN, Bluetooth, LTE, RFID, GSM, GPS, etc. [20–22]. To accommodate multiple standards in a single system, there is a growing need for CMOS PAs with enhanced bandwidth performance [23]. This state-of-the-art review paper provides an overview of the trending research efforts on the development of efficient and linear CMOS PAs with improved bandwidth performance for wireless mobile applications. This paper also discusses the limitations and challenges associated with CMOS PAs and outlines possible directions for future research.

## 2. Performance Metrics of CMOS Power Amplifier

Here, the terminologies and concepts associated with CMOS PAs' performance such as output power, efficiency, stability, intermodulation distortion (IMD), adjacent channel power ratio (ACPR), error vector magnitude (EVM), and amplitude-to-amplitude (AM–AM) and amplitude-to-phase (AM–PM) modulations are presented.

### 2.1. Output Power

Achieving optimal output power in PAs is crucial, and it is a vital parameter that varies depending on the wireless application requirements. For example, to effectively transmit data, cellular applications require a linear output power of 28 dBm [24], while Bluetooth demands a significantly lower output power of 0 dBm [25]. Additionally, the distance of the signal transmission between the transmitter and receiver is directly proportional to the output power level, meaning that a higher output power level results in an extended transmission distance.

An example of this concept is observed in Bluetooth technology, where a Class 1 specification necessitates a linear output power of 20 dBm, resulting in a signal transmission distance of 100 m. In contrast, a Class 3 specification only requires an output power of 0 dBm, limiting the signal transmission distance to 1 m [26]. To determine the output power of the PA, (1) can be utilized with reference to Figure 2, assuming an output load resistance of  $R$ .

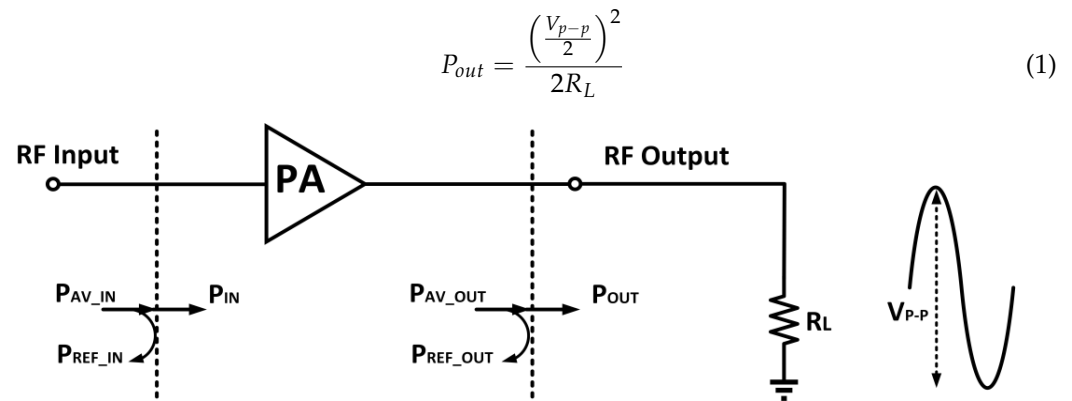


Figure 2. Depiction of an output power definition in a PA.

### 2.2. Efficiency

Efficiency is a crucial factor when it comes to assessing power consumption in PAs. Specifically, the drain efficiency and power added efficiency (PAE) are two commonly used parameters in the evaluation of PAs. In PAs, efficiency represents the amount of DC power that is converted into RF power. The PAE of a PA is a critical parameter that is typically used to assess the efficiency of PAs. In summary, drain efficiency and PAE play significant roles in evaluating the power consumption of PAs. The PAE of a PA is defined as [27]:

$$PAE = \frac{P_o - P_{in}}{P_{DC}} \tag{2}$$

$$\frac{P_o}{P_{DC}} \left(1 - \frac{1}{G}\right) = \eta_D \left(1 - \frac{1}{G}\right) \tag{3}$$

$$\eta_D = \frac{P_o}{P_{DC}} \tag{4}$$

where  $P_o$  is the output signal power,  $P_{in}$  is the input signal power,  $P_{DC}$  is the DC power consumption,  $G$  is the gain of the PA, and  $\eta_D$  is the drain efficiency of the PA. The drain efficiency and PAE are commonly close to each other when the gain of the PA is high.

### 2.3. Stability

In PAs, stability is a crucial parameter, particularly for high-gain PAs. It is worth noting that PAs that are stable under  $50 \Omega$  load terminations may not be stable in realistic wireless environments due to antenna impedance mismatches that occur, such as those caused by nearby objects [28–35]. Therefore, achieving an unconditionally stable characteristic is necessary for PAs to remain stable despite load impedance mismatches [36]. The stability of a PA can be determined from Rollett ( $K$ ), which has to be larger than unity. A PA is unconditionally stable if the value of  $K > 1$ . Meanwhile, if  $0 < K < 1$ , it is considered conditionally stable, and, if  $K < 0$ , it is considered unstable. The  $K$ -factor is defined as

$$K = \frac{1 - |S_{11}|^2 - |S_{22}|^2 + |\Delta|^2}{2 \cdot |S_{11}| |S_{22}|} \tag{5}$$

where

$$|\Delta| = |S_{11} \cdot S_{22} - S_{21} \cdot S_{12}|$$

$S_{11}$  is the input port voltage reflection coefficient,  $S_{12}$  is the reverse voltage gain,  $S_{21}$  is the forward voltage gain, and  $S_{22}$  is the output port voltage reflection coefficient.

### 2.4. Intermodulation Distortion

Due to the non-linearity that exists in the PA, it produces numerous extra terms at innumerable frequencies. The transistors utilized in the PA produce non-linearity due to the non-linear current and non-linear capacitance that rely on the device voltages [37,38]. The main non-linear elements that effect the PA’s performance are the transconductance ( $g_m$ ), drain-source capacitance ( $C_{ds}$ ), and gate-source capacitance ( $C_{gs}$ ) [39]. The Taylor series expansion can be used in order to determine the polynomial transfer function of non-linearity. The significant terms are the first, second, and third orders, which represent the gain, squaring, and cubing functions [40]. The PA’s non-linearity can be delineated by

$$V_o(t) = a_0 + a_1 V_i(t) + a_2 V_i^2(t) + a_3 V_i^3(t) \tag{6}$$

Furthermore, the IMD that represents the linearity performance of a PA is determined by conducting a two-tone signals test in which approximately two spaced fundamental signal tones are supplied at the input of the PA. The amplitude of the two-tone signals is raised up to a certain level in which the third order products generate a signal with a higher amplitude above the noise floor [41–43]. The third order IMD (IMD3) product is the primary concern that needs to be dealt with because it is generated in-band of the fundamental signal frequency. The in-band-generated IMD product is difficult to eliminate using filters. Higher-order IMD products are small in amplitude to induce distortions and can be eliminated using filters [44]. The two-tone signal applied at the PA’s input is given as

$$V_i(t) = v \cos(\omega_1 t) + v \cos(\omega_2 t) \tag{7}$$

Substituting (7) into (6) yields

$$V_o(t) = a_0 + a_1 v [\cos(\omega_1 t) + \cos(\omega_2 t)] + a_2 v^2 [\cos(\omega_1 t) + \cos(\omega_2 t)]^2 + a_3 v^3 [\cos(\omega_1 t) + \cos(\omega_2 t)]^3 \tag{8}$$

From (8), the generated IMD components up to third order are shown in Table 1.

**Table 1.** IMD components.

Order	Terms	$a_1 v^3$	$a_2 v^2$	$a_3 v^3$
0	0		1	
1st	$\omega_1$	1		9/4
	$\omega_2$	1		9/4
2nd	$2\omega_1$		1/2	
	$2\omega_2$		1/2	
	$\omega_1 \pm \omega_2$		1	
3rd	$3\omega_1$			1/4
	$3\omega_2$			1/4
	$2\omega_1 \pm \omega_2$			3/4
	$2\omega_2 \pm \omega_1$			3/4

Thus, the amplitudes of both the upper and lower *IMD3* products are defined as

$$IMD3 = \frac{3}{4} a_3 v^3 \tag{9}$$

Figure 3 illustrates the output power spectrum of a PA subjected to IMD. It can be observed that the upper and lower *IMD3* products are generated in-band approximately to the fundamental tones at  $2\omega_2 - \omega_1$  and  $2\omega_1 - \omega_2$ , respectively.

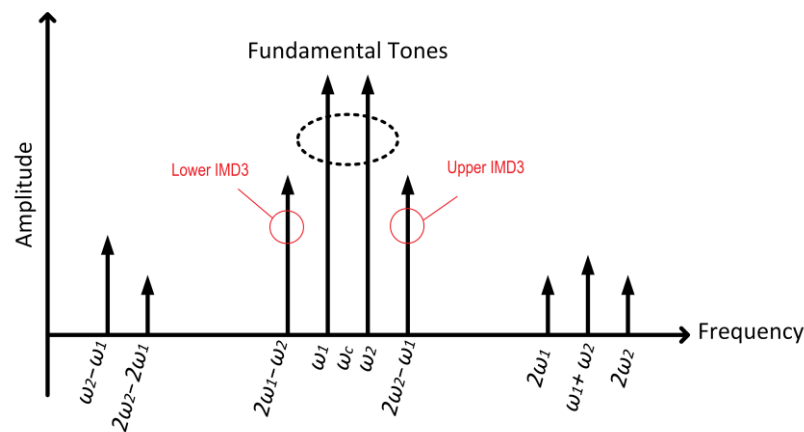


Figure 3. The IMD components induced by a PA.

### 2.5. Adjacent Channel Power Ratio

The adjacent channel power ratio (ACPR) is also a crucial metric that needs attention when a modulated signal is used as the input for the PA [45]. The ACPR values typically depend on the application of the wireless communication. Each wireless standard has adjacent channels located at different frequency offsets. For example, according to the 3GPP standard, the ACLR should be no more than  $-33$  dB at the offsets of  $\pm 1.6$  MHz and no more than  $-43$  dB at the offsets of  $\pm 3.2$  MHz. When a PA is operated with a modulated signal, it generates a bandwidth expansion that is commonly known as spectral regrowth. Spectral regrowth is a form of distortion since it results in adjacent channel interference [46,47]. Figure 4 is an exemplar of the output spectrum that illustrates the phenomena of spectral regrowth.

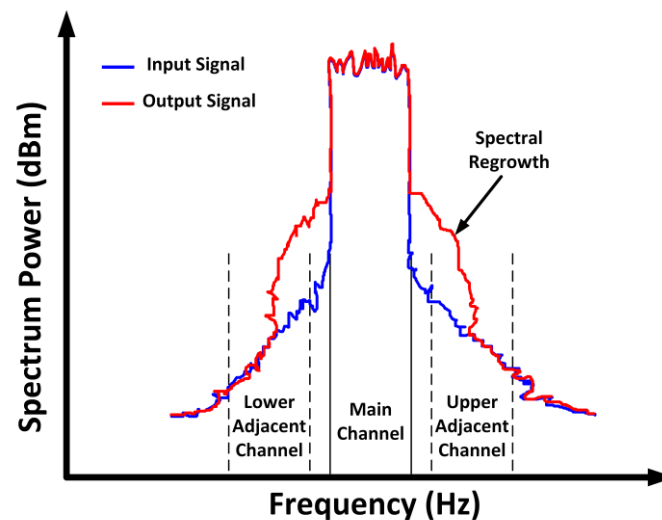


Figure 4. Spectral regrowth of a PA under a modulated signal.

The ACPR is defined in a frequency domain as the power ratio between the distortions in the sideband channels and the signal in the main channel. The ACPR is represented as follows:

$$ACPR_{adj} = 10 \log \frac{\int_{adj} S(f)df}{\int_{main} S(f)df} \tag{10}$$

where  $S(f)$  is the output signal’s power spectral density (PSD), and the term “adj” can be either the first lower or upper channel.

### 2.6. Error Vector Magnitude

Another vital metric to determine the linearity of a PA is the error vector magnitude (EVM). The EVM is a time domain parameter that is represented in terms of a constellation diagram. The rotation and compression of the constellation points are the primary contributor to the constellation distortion, as delineated in Figure 5.

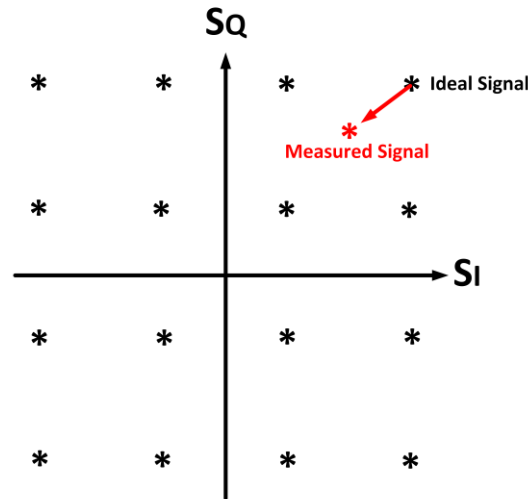


Figure 5. EVM constellation diagram.

The error vector is expressed as the vector discrepancy of the measured and ideal constellation points in the I/Q plane. The EVM is a customary figure of merit (FoM) utilized to interpret the distortions inside the operating band that deteriorate the bit error ratio (BER). The EVM is given as

$$EVM = \sqrt{\frac{\sum_{m=1}^M |S_{ideal,m} - S_{measured,m}|^2}{\sum_{m=1}^M |S_{ideal,m}|^2}} \tag{11}$$

### 2.7. Amplitude-to-Amplitude and Amplitude-to-Phase Modulations

The linearity of the PA can also be determined through the amplitude-to-amplitude (AM–AM) and amplitude-to-phase (AM–PM) modulations. When the PA is subjected to a large-amplitude input signal, the amplitude of the output signal tends to compress, and this decreases the linear output power that can be achieved. Moreover, the phase shift reflects the time delay in which, for an ideal case, it is undeviating at all amplitude levels. However, this is not the case in a real application, since the AM–PM modulation is not constant due to the existing non-linearity. A modulated input signal is expressed as [48]

$$\kappa(t) = A(t) \cdot \cos[\omega_c t + \theta(t)] \tag{12}$$

where  $A(t)$  is the instantaneous amplitude, and  $\theta(t)$  is the instantaneous phase.

AM–AM reflects the interrelation between the output signal’s amplitude and  $A(t)$ . Meanwhile, AM–PM is the interrelation between the output signal’s phase deviation and  $A(t)$  [49]. Hence, the output signal is represented as

$$y(t) = g(A(t)) \cdot \cos[\omega_c t + \theta(t) + \psi(A(t))] \tag{13}$$

where  $g(A(t))$  and  $\psi(A(t))$  are the AM–AM characteristics and AM–PM expression, respectively. The AM–AM and AM–PM characteristics are depicted in Figures 6 and 7, respectively.

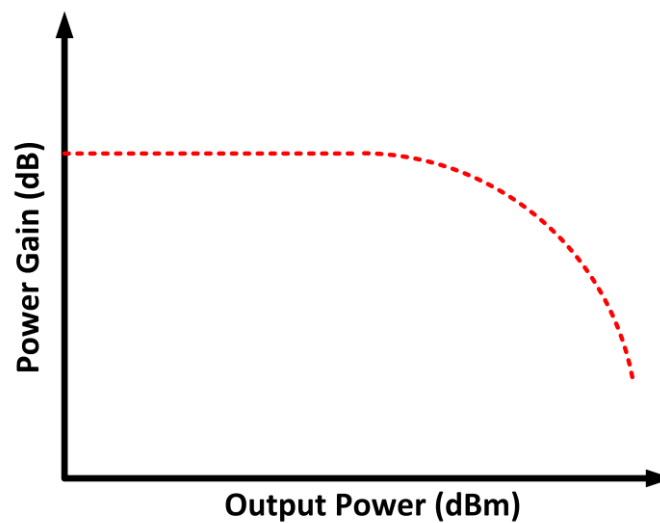


Figure 6. AM–AM feature of a PA across the output power.

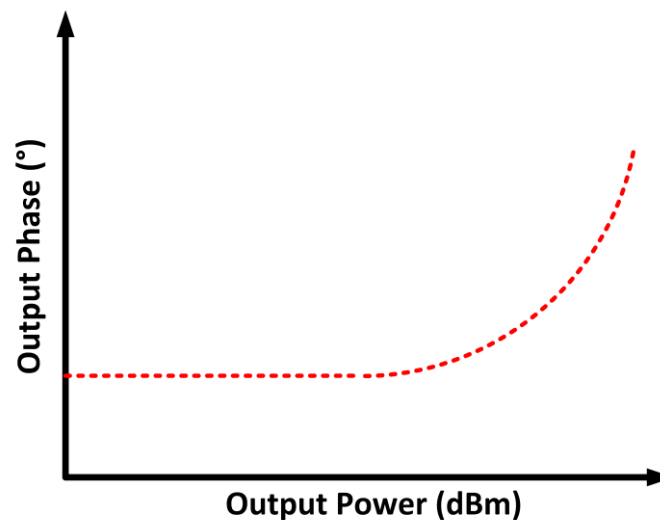


Figure 7. AM–PM feature of a PA across the output power.

### 3. Efficiency Enhancement Techniques

Several techniques were researched and implemented as efforts to enhance the efficiency of CMOS PAs. Commonly utilized efficiency enhancement techniques include the on-chip transformer, Doherty, envelope tracking (ET), envelope elimination and restoration (EER), and out-phasing PAs.

#### 3.1. On-Chip Transformer Power Amplifier

Numerous efforts were applied to utilizing the configurations of on-chip transformers by integrating them together with CMOS PAs. On-chip transformers have various convenient features such as impedance matching, DC isolation, ESD protection, differential-to-single-ended conversion, and single-ended-to-differential conversion. On-chip transformer structures can be classified according to how they are connected. The structures include series combining (voltage mode) and parallel combining (current mode) [50]. The aforementioned structures are delineated in Figure 8.

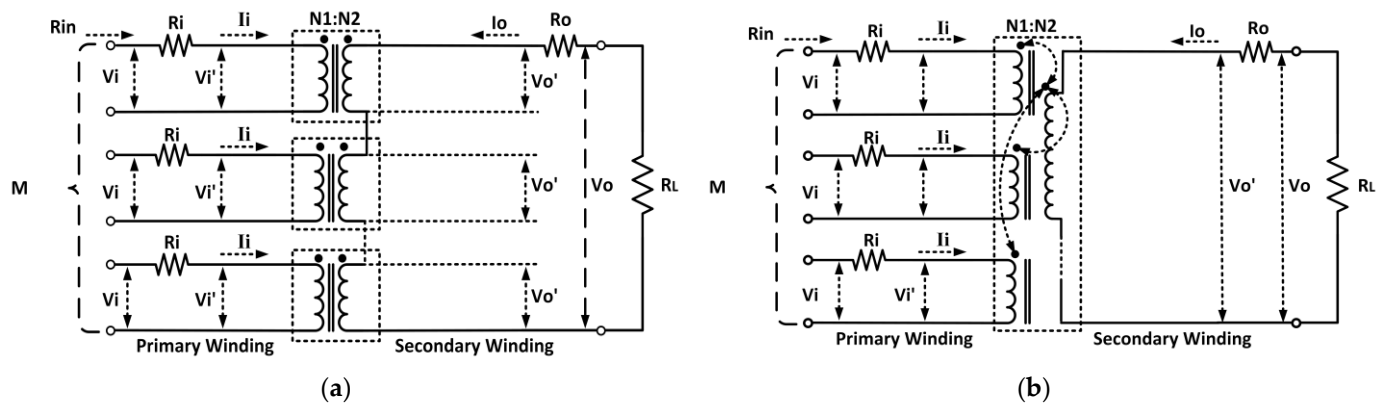


**Figure 8.** (a) Series transformer combination structure. (b) Parallel transformer combination structure.

As the name implies, the series combination transformer has its secondary coils connected in series. The series implementation exhibits a voltage addition on the secondary side, which yields higher output power. This is due to the equal current of  $V_O/R_L$  conducted by the winding of each transformer on the secondary side, as illustrated in Figure 8a [51]. The impedance observed by each amplifier is  $n$  times higher compared to the impedance seen when it is directly connected to  $R_L$ . This is advantageous for the driver amplifier design and for the mitigation of the parasitic effects on the primary side. The transformer has to be highly symmetrical because mismatches could occur, which degrades the maximum efficiency and output power that can be achieved by the PA [52].

By utilizing a series combination transformer, a CMOS PA achieving watt-level output power was proposed by Aoki et al. (2002) [53]. The CMOS PA is employed in a single chip with integrated input and output matching networks. A distributed active transformer (DAT) utilizing a series combining structure is employed for power combining and impedance matching, enhancing the efficiency of the PA [54]. However, the implementation consumes a huge active area on the chip. Meanwhile, a CMOS PA with a smaller footprint was achieved by Javidan et al. (2010) by combining a transformer with different sizes inside each other [55]. The proposed transformer is designed with multiple primary single-turn inductors and a single secondary multi-turn inductor.

The output of multiple PAs can be combined by using a series of combination 1:1 ratio transformers [56]. The output power of the PA can be varied by switching the individual transformers on or off [57]. A. Afsahi et al. (2010) utilized a transformer in order to parallelly combine signals to reduce losses on the secondary side as well as to achieve a better signal symmetry [58]. However, the number of turns in the secondary winding increased, which degrades the self-resonance frequency as well as consumes a huge chip area.

Moreover, K.H An et al. (2007) proposed a monolithic voltage-boosting parallel primary transformer that was utilized for power combining [59]. The transformer gave a voltage-boosting effect by increasing its turn ratio between the primary and secondary windings. An increased current was established in the secondary winding by interweaving multiple primary windings in parallel. An efficient power combining method was achieved by elevating both the secondary voltage and current. An interleaved transformer structure was proposed by A.R. Belabad et al. (2013), which achieved better efficiency compared to a 1:1 ratio transformer [60]. Although the interleaved configuration reduced the Q-factor and self-inductance, it had an enhanced coupling factor that is beneficial for transferring current via its magnetic field. The proposed transformer had two input ports and an output port. The drain terminals of different PAs were connected to the input ports of the transformer while the load was connected to its output port.

Furthermore, H. Ahn et al. (2017) proposed a dual-mode autotransformer-based parallel combining transformer (ABPCT) that provides high efficiency [61]. An individual PA was connected on the secondary side while multiple individual PAs were connected on the primary side. For high-output power operation, all the PAs were turned on. Contrarily,

for low-output power operation, one or two discrete PAs were specifically turned on. The high- and low-power modes were selected by controlling the gate bias of each PAs. Autotransformers have lower power losses due to their reduced total series resistance, which is contributed to by the primary winding that is also a part of the secondary winding. An autotransformer-based PA attained an efficiency of 34% in low-power mode and 38% in high-power mode.

In addition, J. Tsai et al. (2019) proposed a CMOS PA with a transformer-based two-stage dual-radial power splitting and combining mechanism [62]. Several advantages of this proposed transformer included in-phase signal splitting and combining, a compact network, the uniform distribution of DC supplies, and a symmetric supply and return path of the DC current. By utilizing the multi-layer structure of CMOS technology, the radial power splitting plane was implemented on a lower metal layer below the radial power combining plane. This contributed to a compact chip size since both the power splitting and combining shared the same chip area on top of each other. A shielding structure was employed to enhance the isolation between the input radial power splitting and output radial power combining networks. The maximum output power delivered by the PA was 29 to 31 dBm, with a maximum efficiency of 15–25%. J. Tsui (2019) also proposed a 5.3 GHz CMOS PA with a folded radial power splitting and binary power combining on-chip transformer [63]. The proposed architecture of the transformer provided an in-phase signal splitting and combining mechanism. The transformer was also designed with a compact size with uniform DC distribution as well as a symmetric DC current path. At the operating frequency of 5.3 GHz, the CMOS PA achieved a maximum output power of 31.3 dBm, with a peak PAE of 22%.

Another on-chip transformer-based CMOS PA was presented by H. Choi et al. (2020), in which a 1:1 turn spiral transformer balun was implemented with a stacked main PA configuration in order to sustain a high voltage supply [64]. The main PA was constructed in a differential push–pull configuration in order to attain high output power and stability. The 1:1 transformer was employed with an equal coupling line length and an equal inductance in order to achieve an optimum impedance with minimum losses. The proposed CMOS PA also utilized an anti-phase biasing technique to achieve a higher linear output power. The CMOS PA achieved a maximum output power of 29.9 to 30.3 dBm, with 40% to 45% across its operating bandwidth of 0.82 to 1 GHz.

T. Wang et al. (2021) presented an on-chip transformer-based digital CMOS PA in which the transformer acted as a balance-compensated matching network [65]. A series-loaded compensation capacitor was utilized to enhance the balance response of the transformer, which improved the efficiency of the CMOS PA. The transformer was implemented in a four-way series combining configuration. The series combining configuration aided in reducing the voltage stress on the transistors and the impedance transformation ratio of the matching network. The designed transformer was capable of simultaneously providing four-way power combining, balance compensation, wideband impedance matching, and differential-to-single-ended conversion. The proposed CMOS PA delivered a maximum output power of 32.4 dBm at 2 GHz. The maximum drain efficiency achieved was 53.8% at 1.8 GHz.

B. Yang et al. (2021) presented a CMOS PA with a reconfigurable self-coupling cancelling transformer [66]. The proposed transformer had an improved tuning range of the turn ratio that was utilized to boost the PA's efficiency at deep back-off output power. The core of the PA was constructed in a quadrature digital PA configuration with I-Q cell sharing and a hybrid Doherty architecture. The PA also employed a switched/floated capacitor for impedance tuning. The CMOS PA achieved a maximum output power of 30.3 dBm, with 36.6%, the highest system efficiency, at 2.4 GHz. B. Yang et al. (2023) also proposed a watt-level CMOS digital PA using a reconfigurable power-combining transformer [67]. The transformer as employed in a voltage-mode power combining configuration in order to attain high output power across a wide frequency bandwidth. The output power of the CMOS PA at the fundamental signal was further enhanced by using a LC circuit that

suppresses the harmonics. The reconfigurable output matching network was constructed using the power-combining transformer together with four switched capacitors at the inputs and a fixed capacitor and output. Additionally, the dynamic range of the digital PA was enhanced by mitigating the LO leakage by using a 12-bit power digital-to-analog converter (power DAC). The CMOS PA delivered a maximum output power of 32.67 dBm, with a peak PAE of 35.5% at 2 GHz.

### 3.2. Doherty Power Amplifier

The Doherty PA (DPA) was initially proposed by W. H. Doherty, comprising a carrier and a peaking amplifier [68]. A typical block diagram of a classic DPA is depicted in Figure 9 [69]. The back-off efficiency of the PA is improved through its load impedance variation. This is realized by implementing a current source at the output terminal. Figure 10 illustrates the concept of the DPA.

Based on Figure 10, the auxiliary amplifier is denoted by “Aux”, and the main amplifier is denoted by “Main” [70]. The auxiliary amplifier is commonly operated in class C mode while the main amplifier is operated in class AB mode. When the auxiliary amplifier is inactive, the main amplifier faces a load resistance of  $R_L$ . Whereas, if the auxiliary amplifier is active and generates a current,  $I_{aux}$ , the main amplifier, sees a load impedance as

$$Z_{main} = R_{LOAD} \left( 1 + \frac{I_{aux}}{I_{main}} \right) \tag{14}$$

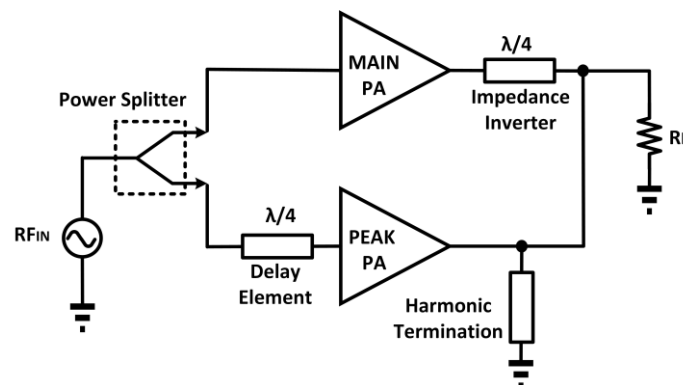


Figure 9. Block diagram of a classic DPA.

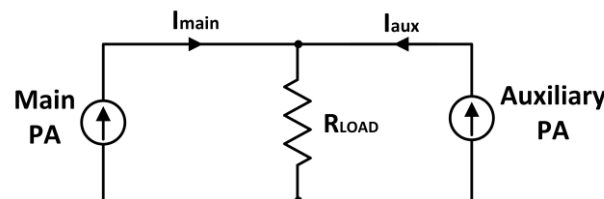
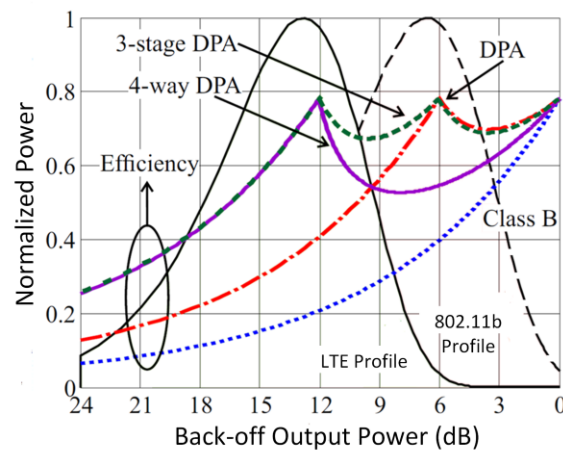


Figure 10. The concept of Doherty PA.

From (14), it is evident that the load impedance of the main amplifier can be varied by controlling the source current of the auxiliary amplifier ( $I_{aux}$ ). This feature of the DPA is utilized to enhance its back-off efficiency, as illustrated in Figure 11 [71]. A constant efficiency across output power was attained by utilizing the DPA technique in CMOS, as presented by N. Deltimple et al. (2015) [72]. S. Hu et al. (2016) proposed a class G DPA that enhances the efficiency at deep back-off output power [73]. A hybrid combo of class G and Doherty improved the deep-back off efficiency without extra complexity at the input and output passive networks.



**Figure 11.** The efficiency profile of DPA.

E. Kaymaksut et al. (2015) presented a CMOS dual-mode Doherty PA with a four-way symmetrical hybrid transformer [74]. The transformer mitigated the impedance imbalance that exists in the PA. The PA employs a switching mode technique with the combination of the Doherty technique, which realizes the high-power and low-power modes. The PA also utilized an adaptive bias circuit that further enhances its linearity and back-off efficiency across its frequency of operation. The proposed transformer utilized the combination of a distributed active transformer (DAT) and a figure-eight-shaped transformer [75,76]. The designed transformer was a  $2 \times 2$  hybrid transformer that utilizes the combination of two DATs with a figure-eight-shaped transformer. In LP mode, only two sub-PAs are switched on, while in HP mode, all the PAs are made active. The PA operates from 1.7 to 2.1 GHz, with a maximum output power of 26–28.2 dBm, as well as a peak efficiency of 25.5–34%. The achieved linear output power was 21–23.4 dBm, with a corresponding efficiency of 16–23.4%.

Further, C.S. Levy et al. (2016) presented a series Doherty PA (SDPA) that is capable of delivering a higher output power than a conventional DPA [77]. In an SDPA, the load voltage is two times higher compared to the voltage of each amplifier separately because of the parallel load impedance of the peaking amplifier. To achieve an efficiency approximate to that of class B operation, the main amplifier is operated in deep class AB operation. In addition, S. Traiche et al. (2017) presented a highly efficient fully integrated CMOS DPA [78]. The proposed DPA comprised a main and an auxiliary amplifier that are operated in class AB and class B, respectively. Both amplifiers utilized the cascode structure to endure the high supply voltage and to achieve high input–output isolation. A Wilkinson divider was used at the input for signal splitting. As for the transmission line, a  $\pi$ -network-based dephasing circuit and impedance inverter were utilized, as well as resonant tanks, to terminate the harmonics.

In addition, D. Jung et al. (2019) presented a Doherty CMOS PA with multi-gated transistors (MGTRs) in the main PA core [79]. This Doherty CMOS PA also employed a class C mode auxiliary PA and a synthesized-transformer-based parallel output network with a second-harmonic control circuit. Each MGTR consisted of four transistors with different sizes and was biased to attain a near-zero third-order transconductance operation. The MGTR and the second-harmonic control circuits both aid in suppressing the third-order intermodulation distortion of the proposed Doherty PA. The MGTR Doherty CMOS PA achieved a maximum output power of 27.2 dBm, with 24.5% PAE at 5.8 GHz.

Y. Yin et al. (2020) proposed a CMOS Doherty PA using digital implementation with a parallel combining transformer for deep back-off efficiency enhancement [80]. The parallel combining transformer offers a dynamic load modulation for the digital Doherty PA in an ultra-compact size. The designed digital Doherty PA consisted of four sub-PAs that are controlled in a precise manner. The load modulation was performed by connecting each of the differential sub-PA pairs to the terminals of the two adjacent primary coils of the power

combiner. The digital Doherty PA delivered a maximum output power of 21.4 dBm, with a peak PAE of 31.3% at 1.5 GHz.

### 3.3. Envelope Tracking Power Amplifier

In an envelope tracking power amplifier (ETPA), a supply modulation mechanism is employed to manage the supply voltage of the PA with the corresponding RF input voltage while maintaining a fixed load resistance [81]. This contributes to the efficiency improvement at the low-output power region by minimizing the power dissipation for systems with a high PAPR [82]. The ET supply modulator tunes the supply voltage level of the PA with respect to the time-varying envelope of the RF input signal in order to keep the PA in stable compression mode. This contributes to the efficiency enhancement of the PA. Figure 12 illustrates the voltage difference between the supply voltage and the RF output signal under a modulated signal [83].

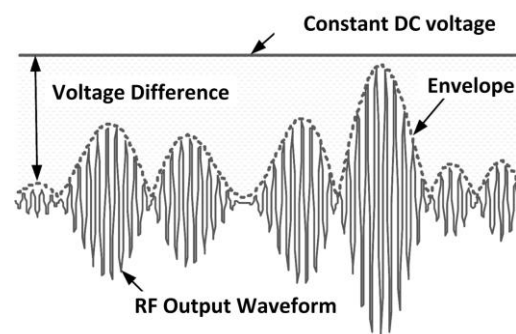


Figure 12. Voltage difference between supply voltage and modulated RF output signal waveform.

An envelope amplifier is utilized for biasing the RFPA according to the input envelope RF signal, as depicted in Figure 13. An envelope detector on the input path is employed to retrieve the envelope information. The envelope information can also be retrieved by utilizing digital baseband processing [84].

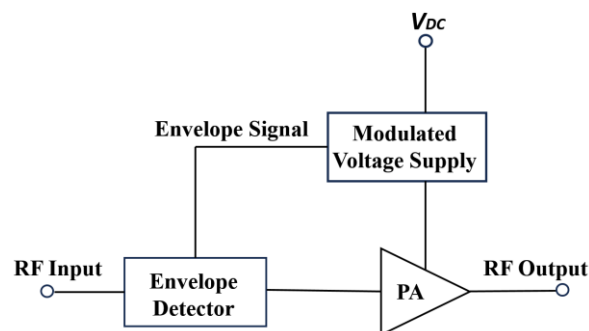
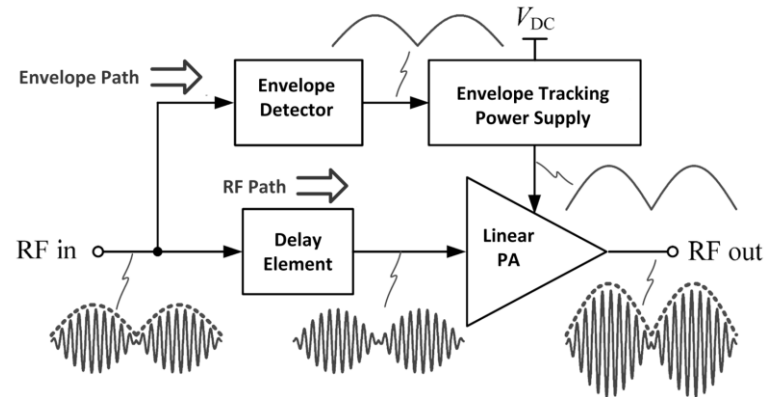


Figure 13. Block diagram of the ETPA.

Figure 14 depicts the block diagram of an ETPA together with its relative waveforms. The ET method is commonly integrated with a linear power amplifier (LPA), and the RF signal amplified contains both the amplitude and phase information. The power supply in an ETPA is mainly focused on enhancing the efficiency of the PA, and its overall efficiency includes both the efficiency of the PA and the envelope amplifier.

J. L. Woo et al. (2014) introduced a dynamic stacked CMOS ETPA that achieved high efficiency during low-output power operation [85]. The proposed ETPA achieved high efficiency by utilizing a 3.4 V maximum voltage. Furthermore, B. Park et al. (2016) proposed an ETPA with an improved ET supply modulator [86]. By integrating this supply modulator, an enhanced efficiency was achieved at all output power levels. There were also second-order harmonic control mechanisms employed at the input and output of the ETPA that further improved its efficiency. Moreover, an ETPA with a dual-mode supply

modulator was presented by Ham et al. (2016) [87]. A dual-mode supply modulator was utilized for envelope tracking and average power tracking. This modulator was designed based on a hybrid buck converter comprising switching and wideband linear amplifiers. This ETPA achieved a peak efficiency of 45.4% under the envelope tracking mode.



**Figure 14.** Key waveforms in an ETPA.

### 3.4. Envelope Elimination and Restoration Power Amplifier

The envelope elimination and restoration (EER) technique was introduced by L. R. Khan in 1952 [88]. Contrary to ETPA, the EER technique is implemented in a non-linear PA (NLPA). EER adopts a supply modulation method in which it splits the RF modulated signal into envelope and phase signals and later combines it at the output of the NLPA. A high-speed supply modulator is employed for the supply voltage modulation of the NLPA. Figure 15 delineates the block diagram of an EERPA together with its key waveforms.

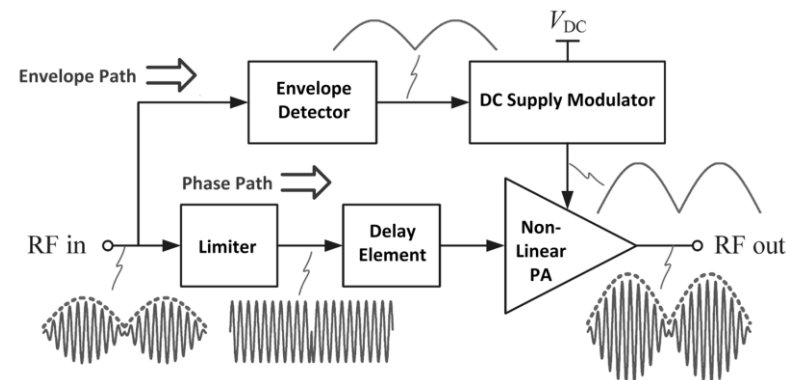


**Figure 15.** Key waveforms in an EERPA.

Referring to Figure 15, the RF input signal that consists of amplitude and phase information is handled by two different paths, which are the envelope and phase paths. At the envelope path, the input signal's envelope is identified by the envelope detector and is utilized as the reference voltage for the supply modulator. The supply modulator then generates an output voltage that follows the input signal's envelope and supplies the voltage to the NLPA. In contrast, at the phase path, the limiter is utilized to eliminate the input signal's envelope information and generate a constant amplitude signal with only the phase information. The amplitude information is restored by the supply voltage given by the supply modulator. The delay unit is utilized to synchronize both the envelope and phase paths.

A. Mamdouh et al. (2020) presented a fast transient supply modulator for an EERPA [89]. The efficiency was improved at a high frequency due to the fast transient response of the supply modulator compared to conventional hybrid mode supply modulators. K. Oishi et al. (2014) proposed an EERPA with an envelope/phase generator based on a mixer and a limiter that generates a wide-bandwidth phase signal [90]. A delay locked

loop-based timing aligner was implemented with a variable high-pass filter to compensate for the timing mismatch. Furthermore, W. Yuan et al. (2015) explored a digital-based implementation and proposed an EERPA with a class E configuration and a digitally controlled current DAC modulator [91]. A switched capacitor-based DAC was presented to control an open-loop transconductor that serves as a current modulator. The current modulator modulated the amplitude of the current supplied to the class E configured PA.

X. Liu et al. (2019) proposed an EER envelope-shaping PA with an AC-coupling supply modulator [92]. The supply modulator comprised a 25 MHz three-level switching amplifier and a wideband-assisting linear amplifier. The AC-coupling method utilized the shaped envelope to mitigate the power consumption of the linear amplifier and generate a higher voltage than its supply. A high-efficiency, small-output voltage ripple and a fast transient response were achieved by implementing a switching amplifier with three-level real-time flying capacitor calibration. A multi-loop control was utilized in order to further increase the switching amplifier speed and, thus, enhance the overall efficiency. As for the PA, a mode-switching PA was implemented in a differential cascode structure, and bond wires were utilized as its DC-feed inductor. To improve its efficiency, the common-gate voltage of the cascode PA was dynamically biased with respect to the instantaneous supply voltage. A capacitive-charging-acceleration method was also implemented to further increase the efficiency [93]. The supply modulator achieved an efficiency of 88.7%, while the overall EERPA achieved an efficiency of 35.7%.

### 3.5. Out-Phasing Power Amplifier

An out-phasing PA utilizes the method of separately splitting and amplifying the signals then combining them at the output. The signal with amplitude modulation is given as the vector sum of two constant envelope phase-modulated signals. An improved efficiency is achieved by modulating the differential phase while keeping the amplitude of the input signal constant. For out-phasing techniques utilizing non-linear components, amplitude modulation is conducted by combining the outputs of two PAs THAT are supplied with constant envelope phase-modulated signals [94–98]. The architecture of the out-phasing technique is shown in Figure 16, and its principle of operation is depicted in Figure 17.

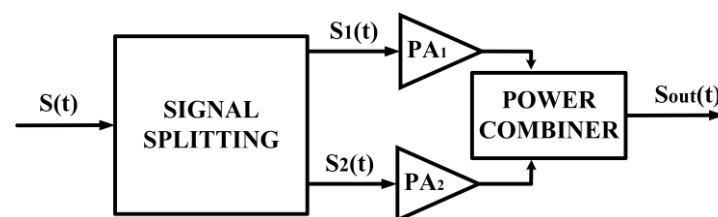


Figure 16. Architecture block diagram of out-phasing.

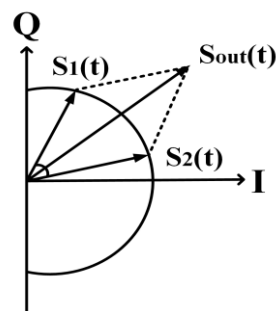


Figure 17. Operation principle of out-phasing.

A modulated signal can be represented, as shown in (15), and its amplitude and phase can be split into two constant amplitude and phase-modulated signals ( $S_1(t)$  and  $S_2(t)$ ), as shown in (16) and (17).

$$S_{out}(t) = A(t)\cos(\omega_c t + \varnothing(t)) \quad (15)$$

$$S_1(t) = \frac{A_{max}}{2}\cos(\omega_c t + \varnothing(t) + \theta(t)) \quad (16)$$

$$S_2(t) = \frac{A_{max}}{2}\cos(\omega_c t + \varnothing(t) - \theta(t)) \quad (17)$$

where  $S_{out}(t) = S_1(t) + S_2(t)$ ,  $A(t)$  is the time-dependent amplitude, and  $\varnothing(t)$  is the time-dependent phase of the original signal,  $S(t)$ ;  $\omega_c$  is the angular frequency of the carrier, and  $A_{max}$  is the maximum value of  $A(t)$ . The angle  $\theta(t)$  is defined as

$$\theta(t) = \cos^{-1} \frac{A(t)}{A_{max}} \quad (18)$$

Since  $S_1(t)$  and  $S_2(t)$  are constant envelope phase-modulated signals, the signal amplification can be conducted by utilizing a non-linear PA. The outputs of the PA can be joined by using a combiner circuit in order to obtain  $S_{out}(t)$ .

Z. Hu et al. (2016) proposed an RFDAC-based out-phasing PA with an integrated combiner [99]. Increased efficiency was achieved by utilizing a dynamic amplitude control in a quasi-load insensitive class E configured PA. The amplitude was controlled through a digitally divided method for the branch amplifier. Highly reactive and severe load modulation conditions were avoided through this method, which contributed to the minimization of power losses.

Furthermore, a CMOS class D configured multi-level out-phasing transmitter with on/off control logic method was presented by M. Martelius et al. (2016). The PA consisted of eight individual amplifiers with cascoded output stages [100]. The PAs were selectively activated in pairs to achieve different amplitude levels as a means of improving the back-off efficiency. A. Banerjee et al. (2017) proposed a CMOS class E configured out-phasing PA with a novel passive combining circuit [101]. The designed passive combining circuit contributed to achieving enhanced output power and efficiency. The combiner comprised a power enhancement circuit and an efficiency enhancement circuit integrated together. Moreover, A. Ghahremani et al. (2018) presented a class E out-phasing PA by conducting load-pull analyses [102]. These load-pull analyses were carried out to rotate and shift the power and efficiency contours. This method was utilized to improve the efficiency at deep back-off output power. The rotation of the power and efficiency contours were realized by tuning the LC tank's resonance frequency and duty cycle scaling factor. This class E PA consisted of transistors that serve as a square-wave input-signal-driven switch with a duty cycle of 50%. Parallel bond-wires with a high Q-factor were utilized as the DC-feed inductors for each PA. The cascade inverters employed in the PA were used as a driver for the switch. The duty cycle of the switch was controlled by using the off-chip control voltage. The switch capacitor banks were used to vary the resonance frequency of the LC tank at the switching nodes.

M. Martelius et al. (2020) proposed an out-phasing CMOS PA with the combination of a polar mechanism that implements a tri-phasing modulation [103]. The combination of the polar and out-phasing components mitigated the linearity-degrading effects while maintaining the back-off efficiency. The CMOS PA comprised eight class D units on a single chip. The power combiner of this CMOS PA was implemented using Marchand baluns that consist of input transmission lines and coupled-line architecture on a printed circuit board. This CMOS PA achieved a maximum output power of 29.7 dBm, with a peak PAE of 34.7% at 1.7 GHz.

A. Banerjee et al. (2020) presented a multi-mode class E out-phasing CMOS PA with an integrated passive combining circuit [104]. Multiple class E PAs were turned ON and OFF in

order to configure the efficiency of the PA at low power levels. This out-phasing CMOS PA also utilized an efficiency enhancement circuit (EEC) which further assisted in improving the efficiency at back-off output power. In an out-phasing PA, the in-phase components are added together and increase the load power, while the out-of-phase components cancel each other out and reduce the load power. In order to enhance the back-off efficiency, the power loss due to the out-of-phase components should be minimized without trading off the in-phase operation. Thus, an EEC is employed for this purpose. The proposed EEC is realized using an inductor that is connected between the drains of the main PAs. Table 2 summarizes the recent state-of-the-art CMOS PAs with efficiency enhancement techniques.

**Table 2.** Summary of the recent state-of-the-art CMOS PAs with efficiency enhancement techniques.

Architecture	Year	Tech (nm)	V <sub>DD</sub> (V)	Freq. (GHz)	Max. P <sub>out</sub> (dBm)	Peak PAE (%)	Ref.
On-Chip Transformer	2010	180	3.3	0.9	29.5	24.0	[55]
	2010	65	3.3	2.4	33.5	37.6	[58]
	2013	180	3.3	2.4	32.5	37.9	[60]
	2017	40	2.8	1.75	24.7	38.1	[61]
	2019	180	5.0	5.2	30.1	22.2	[62]
	2019	180	3.3	5.3	31.3	22.0	[63]
	2020	180	4.6	0.82–1.0	30.3	45.0	[64]
	2021	40	2.5	1.2–2.8	32.4	53.8	[65]
	2021	40	2.4	2.4	30.3	36.6	[66]
	2023	40	2.5	2.0	32.67	35.5	[67]
Doherty	2015	65	2.5	2.5	23.4	24.7	[72]
	2016	65	3.0	3.71	26.7	40.2 *	[73]
	2015	40	1.5	1.7–2.1	28.2	34.0	[74]
	2016	45	2.4	14.0	22.0	24.0	[77]
	2017	130	2.6	3.0	26.0	48.0	[78]
	2019	55	5.5	5.8	27.2	24.5	[79]
	2020	40	1.1	1.5	21.4	31.3	[80]
ETPA	2014	320	3.4	0.837	25.9	47.5	[85]
	2016	180	4.7	1.7	28.5	36.6	[86]
	2016	180	3.3	0.78	24.0	45.4	[87]
EER	2020	130	3.0	1.0	26.5	79	[89] <sup>+</sup>
	2014	90	3.3	1.95	28.0	39	[90]
	2015	130	2.5	2.4	22.5	23.6	[91]
	2019	65	2.4	2.4	23.9	35.7	[92]
Out-phasing	2016	40	1.2	5.9	22.2	49.2 *	[99]
	2016	28	3.6	1.8	32.4	34.1	[100]
	2017	45	2.4	2.4	29.5	46.8 *	[101]
	2018	65	1.25	1.8	20.1	60.7	[102]
	2020	28	3.6	1.7	29.7	34.7	[103]
	2020	45	2.4	2.4	31.6	49.2 *	[104]

\* drain efficiency; <sup>+</sup> simulated.

Figure 18 delineates the plot of the PAE achieved by the aforementioned techniques across the achieved output power. The proposed techniques are capable of delivering a maximum output power of more than 20 dBm. It can be observed from Figure 18 that the on-chip transformer and the out-phasing techniques are capable of delivering watt-level maximum output power for CMOS PAs. This is due to the usage of power-combining architectures in these techniques that boost the maximum output power. The PAE achieved by these techniques was mostly more than 30%. The highest PAE was achieved by using the EER technique; however, the research was limited to only simulated data.



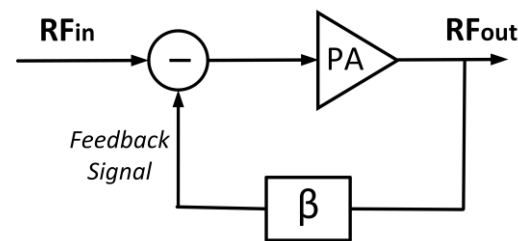


**Figure 19.** Principle of feedback technique.

#### 4.1.1. Cartesian Feedback Technique

Cartesian feedback is a technique that encompasses the linearization of the overall transmitter system. In the Cartesian feedback method, the baseband I and Q signals are upconverted to the carrier frequency, and the signals are then amplified. The signals are later sampled and downconverted back into the quadrature component, which is connected back to the input of the transmitter.

Error amplifiers are employed to compare the signal to the original baseband input signals [113]. The delay that exists in the feedback loop limits the bandwidth of the transmitter. Figure 20 depicts a simple block diagram of a Cartesian feedback implemented in a PA [114].

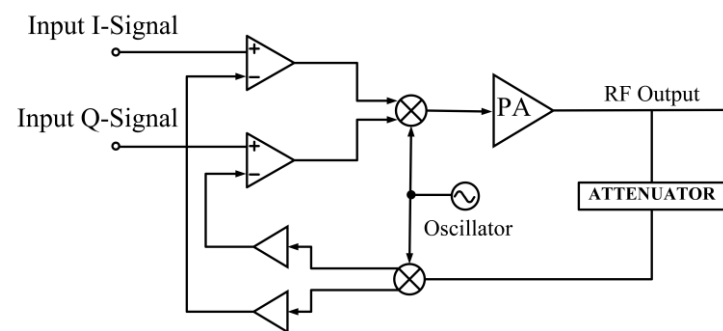


**Figure 20.** Cartesian feedback technique.

L. Tee et al. (2006) presented a Cartesian feedback implemented in a CMOS PA for EDGE application [115]. The PA comprised a pre-driver, a driver, and a main amplifier. The main amplifier was operated in class C, which attained high efficiency. A class AB transistor was integrated with the class C amplifier to achieve stability at all input levels at the output stage. Furthermore, a Cartesian feedback linearization for CMOS Zigbee PA was proposed by A. Atres et al. (2016) [116]. A class E operation was adopted to obtain a high efficiency. The PA was tested with  $\pi/4$  DQPSK modulation at 868 MHz in order to verify its linearity performance. A resistor was used at the input matching network to improve the stability of the PA. An inductor and a capacitor connected in series in the output matching network were utilized for waveform shaping. The employed Cartesian feedback system was capable of lowering the spectral regrowth at the adjacent channels.

#### 4.1.2. Polar Feedback Technique

Unlike a Cartesian feedback, which feedbacks the I and Q data, the polar technique feedbacks the amplitude and phase into the input of the system. The difficulty with this approach is that the feedback bandwidths of the amplitude and phase components are different from each other. This deteriorates the available loop gain to either the amplitude or phase path because one path needs a feedback bandwidth that limits the loop gain, while the other path requires a larger loop gain. Figure 21 shows the block diagram of a polar feedback system that addresses both amplitude and phase distortion with separated loops [117].

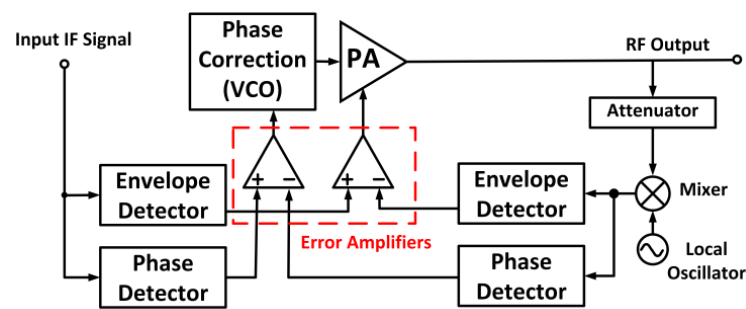


Figure 21. Block diagram of a polar feedback system.

In the polar feedback technique, a local oscillator and a mixer are employed to attenuate and downconvert the output signal of the PA. The downconverted output signal is compared with the envelope of the incoming intermediate frequency (IF). Moreover, the error amplifiers in the negative feedback loop are employed to control the bias condition of the PA.

A polar transmitter with a current-mode class D CMOS PA was presented by T. Nakatani et al. (2013). This polar transmitter also consisted of a digital pulse width modulation (DPWM) algorithm that was employed to mitigate spurious signals linked with the digital input signal envelope [118]. DPMW was mainly employed to minimize the noises induced by the clock via a minimum quantization error dithering (MQED) method. This approach spreads out clock spurs, reduces quantization errors, and mitigates peak spurs.

Further, S. Zheng et al. (2013) presented a digital polar transmitter comprising a six-bit CMOS PA array [119]. The proposed design employed a highly linear charge-mode switched-capacitor digital polar modulator (DPM) in place of the conventional switched-current DPM. A cascode common-source configuration in the differential structure was utilized in the PA. The replica of the main PA was integrated with a comparator and a resistor. The replica was employed to regulate the main PA's bias level with an analog feedback loop in which it mitigated the AM path's distortion.

#### 4.2. Feed-Forward Technique

Feed-forward linearization is employed to mitigate distortions at the output of the PA. The feed-forward technique focuses on the subtraction of the harmonics and intermodulation components from the output spectrum of the PA [120]. Feed-forward comprises two cancellation loops based on two amplifiers: the main amplifier and the error amplifier. Figure 22 shows the block diagram of a feed-forward-based PA. The input signal is split into two, in which one portion is amplified via the main PA, and another portion is processed via the delay element. The feed-forward method is advantageous for wideband linearization, but it increases the implementation cost and circuit complexity.

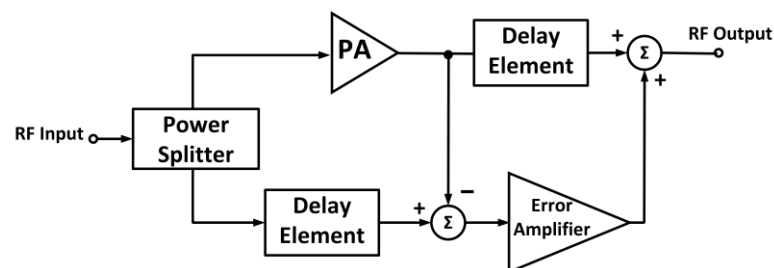


Figure 22. Block diagram of the feed-forward-based PA.

The feed-forward approach was realized in a 24 GHz cascode CMOS PA, as demonstrated by Y. H. Chen et al. (2015) [121]. The PA employed a successive second-order intermodulation (IMD2) feed-forward cancellation. The main path comprised a cascode PA operated in class AB, while the auxiliary path comprised successive IMD2-generating common-source amplifiers. The transistors in the common-source amplifiers were operated in the class B region, in which it detected the fundamental signals and generated the maximum IMD2 components and moderate fundamental components. Further, the transistor in the final stage generated IMD3 components that were utilized to cancel the main path's IMD3 components. A diode-connector-based level shifter was employed at the final stage in order to realize the biasing voltage in class B and also to allow the very-low-frequency signals to pass through. The PA was capable of effectively mitigating the IMD3 by reducing the third-order transconductance, which is the major contributor to IMD3. The IMD3 value was enhanced by 20 dB at the "sweet spot" located at an output power of 5 dBm, with the auxiliary stage being active. The IMD3 measurement was carried out with a 1 MHz spacing two-tone test at 24 GHz, while the ACPR measurement was completed with 64 QAM, at a 1 MHz symbol rate.

#### 4.3. Linear Amplification Using Non-Linear Components Technique

The linear amplification using non-linear component (LINC) is usually employed with highly efficient PAs such as class C, D, E, or F. In LINC, the modulated input signal is split into constant envelope and phase-modulated signals. These signals are independently amplified by two PAs with the same features. The two amplified signals are later combined together at the output with fewer distortions [122]. The separated signals are constant envelope, thus they are insensitive to the non-linearity of the PAs. Therefore, the employment of non-linear switching-mode PAs is advantageous when implemented in LINC techniques. Figure 23 illustrates the typical block diagram of a LINC technique.

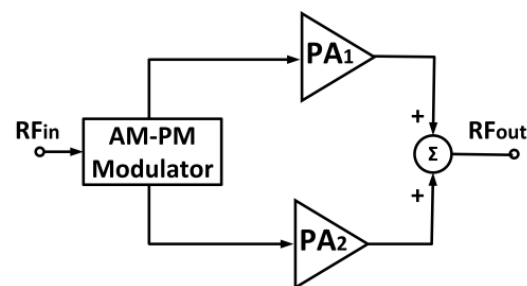


Figure 23. Block diagram of LINC technique.

H. Lee et al. (2010) presented a multi-mode LINC PA that was employed with a differential two-pair class AB CMOS PA [123]. The PA comprised two pairs of driver stages and main power stages that employed a cascode structure and stabilizing feedback circuits. The multi-mode LINC PA was capable of enhancing its linear output power by 7% and its efficiency by 8% compared to the conventional method. H. Lee et al. (2013) also presented a hybrid polar-LINC PA that employed a combination of polar and LINC mechanisms [124]. This hybrid polar-LINC PA was configured in a differential structure comprising two pairs of driver stages and power stages and an output combiner. The driver and power stages were both based in class E operation. The proposed power combiner comprised a transmission line transformer (TLT) with isolation resistors. The employed isolated TLT avoided distortion induced by the mutual load-pulling effects, which occur in non-isolated combiners [125]. The isolated combiner allowed a more linear and precise signal combination that resulted in ACLRs of  $-36$  dBc and  $-47$  dBc under 5 MHz and 10 MHz WCDMA signals, respectively.

#### 4.4. Pre-Distortion Technique

Pre-distortion employs an approach of intentionally introducing distortions in terms of amplitude and phase that are in contrast to a PA's distortion [126]. This results in the cancellation of distortions and, thus, enhances the linearity. The pre-distortion technique provides a wide-bandwidth operation due to its open-loop feature, which makes it advantageous over feedback techniques [127]. Pre-distortion is also advantageous over the feed-forward technique due to its simplicity and low power consumption [128]. The pre-distorter mechanism is implemented at the input of the PA, as shown in Figure 24. Pre-distortion is highly flexible, effortlessly reconfigurable, and suitable for wideband application. However, the PA's characteristics' variation is subjected to component tolerances. The pre-distortion mechanisms can be employed in an analog or digital manner.

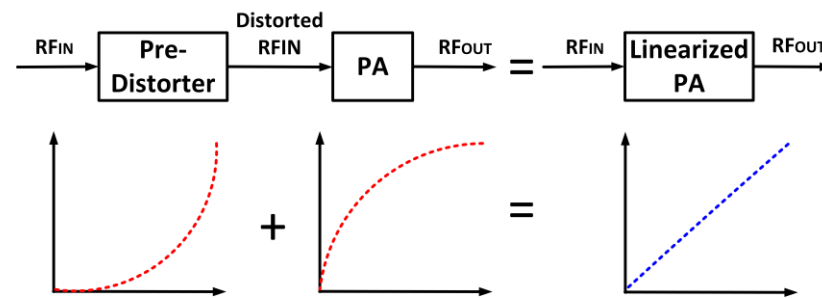


Figure 24. The concept of pre-distortion.

##### 4.4.1. Analog Pre-Distortion Technique

Analog pre-distortion (APD) employs a non-linear mode device to pre-distort the input signal prior the PA. RF pre-distortion is usually implemented in an analog mechanism due to the complexity of the sampling frequency needed to be digitally processed.

K. Y. Son et al. (2012) proposed a CMOS PA with an integrated digitally controlled APD [129]. This APD had two external digital control words, which are the I-path and Q-path control words. These digital control words were utilized to control the AM–AM and AM–PM distortions in the PA. The driver stage of the PA was employed in a vector modulator manner, so the gain and phase can be varied via the vector sum method [130,131]. The linear output power of the PA was enhanced by 6.5% with this approach. Furthermore, a 15 GHz DPA with an integrated APD as presented by N. Rostomyan et al. (2018) [132]. The main and peaking paths were both constructed with two-stage amplifiers. In the input and output power combiners, high-pass  $\pi$ -networks were utilized due to their advantages in terms of stability and a compact area compared to a  $\lambda/4$  transmission line. The APD in this design focused on the gain non-linearity issue of a symmetrical DPA. The linear output power and gain flatness were achieved by controlling the supply and bias voltages of the envelope detector employed in the PA. An improvement of 9.1% in the linear output power was observed via the implementation of the proposed APD.

Furthermore, S. Mariappan et al. (2021) presented a CMOS PA with a wideband pre-distortion (WPD) mechanism that consisted of a hybrid feedback with both active and passive networks [133]. The WPD provided both gain and phase cancellation schemes that aid in mitigating the third-order intermodulation product. The WPD exhibited a capacitive response that is in opposition to the main PA's inductive response. An active load was implemented at the WPD instead of an RF choke, which generated the capacitive response. The proposed CMOS PA with WPD achieved a maximum output power of 24 dBm, with a peak PAE of 35.5% at 2.45 GHz. The achieved linear output power was 20 dBm across the operating frequency bandwidth of 0.8–3.3 GHz. S. Mariappan et al. (2021) also presented a CMOS PA with a broadband pre-distortion (BPD) that used the same aforementioned mechanism [134]. However, this CMOS PA as implemented on a Roger's RO4000/FR4 PCB, which achieved a maximum linear output power of 21 dBm across the frequency bandwidth of 0.4–2.8 GHz. The peak efficiency achieved is more than 35%.

S. Mariappan et al. (2021) proposed another CMOS PA with an integrated digitally assisted analog pre-distorter (DAAPD), which offers a reconfigurable linearization scheme [135]. The DAAPD was utilized to tune the interstage load impedance between the driver stage and the main stage. The load impedance was reconfigured by varying the transconductance of the driver amplifier and its respective active load. The DAAPD consisted of a digital bias controller that comprised a seven-stage voltage generator with a band-gap reference voltage, buffer, and op-amp, which was employed to provide the biasing voltage that controls the transconductance. The DAAPD was also employed to optimize the process–voltage–temperature variation in the CMOS PA that contributes to its robustness. The DAAPD generated a capacitive response as opposed to the inductive response of the main PA that enhances the linearity. This CMOS PA exhibited a maximum output power of 27–28 dBm across the frequency bandwidth of 1.7–2.7 GHz. The linear output power achieved was 24–25 dBm.

Based on the aforementioned design, S. Mariappan et al. (2023) further improved the presented design by proposing a reconfigurable CMOS PA with digital linearizers and a tunable-output impedance matching network for PVT robustness [136]. The digital linearizer was implemented at the driver stage of the CMOS PA, which acted as the wideband pre-distorter. The tunable-output matching network was realized via an interleaved planar transformer with a switched capacitor at both the primary and secondary windings. The switched capacitor was capable of maintaining the efficiency and the output power of the CMOS PA across its operating frequency bandwidth as well as PVT, while the digital linearizer conducted the linearization tuning. The proposed mechanisms for the CMOS PA achieved a linear output power of 24–25 dBm and a PAE of 34.5%–38.8% across the frequency of 1.7–2.7 GHz.

In addition, J. Tsai (2023) proposed a CMOS PA with a high-power APD constructed with a cascode cold-FET [137]. The CMOS PA was comprised of three differential main PA units, a driver amplifier, a two-stage dual-radial power splitter/combiner and a pre-distorter as the linearizer. The cascode cold-FET had a higher breakdown voltage that can sustain a higher input power and generated a larger gain expansion region compared to conventional common-source cold-FET implementation. This allowed the APD to conduct linearization at a higher-output power region and further enhanced the linear output power of the proposed watt-level CMOS PA. The proposed CMOS PA operated at 5.3 GHz, with a maximum output power of 30.1 dBm and a peak PAE of 18%. The achieved linear output power was 21 dBm after linearization was conducted.

#### 4.4.2. Digital Pre-Distortion Technique

The digital pre-distortion (DPD) technique is gaining popularity due to the rapid development of digital signal processing (DSP) [138]. Due to the limitations in terms of complexity, cost, and efficiency, the DSP-based DPD is restricted to less than a 100 MHz operation bandwidth. The DPD mechanism is commonly implemented with direct and indirect learning architectures [139–141].

Y. Cho et al. (2014) presented a CMOS DPD PA with an off-chip open-loop DPD algorithm that only uses a single look-up-table (LUT) [142]. The DPD was employed for a large dynamic range of output power via a LUT-based average output power control. An enhancement of 8 dB was achieved in ACPR by utilizing the proposed DPD.

Moreover, a two-core digital CMOS PA with on-chip integrated DPD was presented by A. Wong et al. (2017) [143]. A polar architecture and an on-chip 1-D LUT were employed in the proposed design. The digital PA adopted a double cascode configuration. The NAND gates were employed to drive the device's transconductance with inputs of amplitude and phase switching at the rate of the carrier frequency. The amplitude data were obtained via the on-chip DSP in four 12-bit data streams at a rate of one-fourth of the carrier frequency. On the other hand, the phase data were obtained via two sets of four parallel 10-bit data streams that were converted into two series of 10-bit data streams before they were supplied into the I-Q DAC. A piecewise linear DPD was employed in this design, which achieved

linear output power of 26.8 dBm and 25 dBm for the 20 MHz 802.11g and 40 MHz 802.11n signals, respectively.

#### 4.5. Adaptive Biasing Technique

Linearization can also be conducted by controlling the transconductance of the CMOS PA. Since this transconductance is directly dependent on the gate voltage of the transistor, adaptive biasing circuits are extremely beneficial for this implementation. They only provide a variable bias current when an input signal is present. In the absence of such input, they provide a constant, precisely controllable quiescent current. In this manner, the quiescent power consumption is decreased without compromising the transient performance.

W. Kim et al. (2014) proposed a CMOS PA with an adaptive biasing technique for EDGE/GSM application [144]. To improve the AM–AM characteristics, this CMOS PA was adaptively biased according to its input power level. The adaptive bias circuit was designed to enhance bias voltages when the input signals were large, thereby increasing the 1 dB output power in proximity to the peak power. Also, the non-linear gate–drain capacitance ( $C_{gd}$ ) of the power transistors, which is a primary source of AM–PM non-linearity, was effectively linearized by adding a series capacitor. The proposed CMOS PA achieved PAEs of 22% and 23% at linear output powers of 28.5 dBm and 27.5 dBm, at 870MHz and 1.8 GHz, respectively.

H. Kim et al. (2015) introduced a CMOS PA with the implementation of a dynamic bias switching method via digital control [145]. The digital signal processing unit generated the control signal for the bias switching operation based on the amplitude of the envelope signal. The dynamic bias switching circuit provided dual supply voltages to the PA's drain. The dynamic bias switching circuit produced a low supply voltage through the use of a DC–DC converter, whereas the high voltage can be directly sourced from the power supply. The compensation of the gain difference between low- and high-bias voltage conditions was implemented to enhance the linearity of the CMOS PA. The optimization of the threshold voltage for the envelope signal and the low supply voltage level was carried out through analytical means to achieve the highest possible efficiency without trading off its linearity. This was achieved by utilizing the envelope statistics of the LTE signal. This CMOS PA achieved a linear output power of 22 dBm, with a peak PAE of 34.5% at 1.75 GHz.

B. Kim et al. (2016) proposed a CMOS PA using the reconfigurable adaptive power cell technique. This CMOS PA was configured in a cascode structure that consisted of four differently biased power cells to achieve high linearity [146]. Out of the four power cells, two of them were shut off to operate the CMOS PA at a high frequency. This made the CMOS PA operate at a dual-frequency band. The power cells were designed with different channel widths that give different input average capacitances. Therefore, the total average capacitance variation with regard to the input power may become relatively insignificant as a result of mutual cancelling, which contributes to enhancing its linearity. The maximum output power attained was 27.8 dBm, with a peak PAE of 52.5%. This CMOS PA achieved a linear output power of 17.5 dBm at 650 MHz.

Furthermore, J. Ren et al. (2020) introduced a CMOS PA with an adaptive bias circuit that generated a precise biasing voltage according to the input envelope RF signal [147]. This CMOS PA also employed harmonic termination circuits at the gate of the common-gate PA and the center-tap node of the output transformer. The harmonic termination aided in shorting the second-harmonic components to the ground, which further enhanced the linearity. This CMOS PA achieved a maximum output power of 30.3 dBm, with a peak PAE of 43.1% at 2.4 GHz. The achieved linear output power was 23.5 dBm, with 18.1% linear efficiency.

S. Mariappan et al. (2021) presented a dual-stage CMOS PA with adaptive biasing in which the gate voltage of the driver amplifier was adaptively tuned to be in opposition to the third-order transconductance response compared to the main PA [148]. The biasing voltage was supplied through a current-mirror configured biasing circuit. The opposite third-order transconductances between the stages cancel each other by assisting in mitigating the

third-order intermodulation product. This proposed CMOS PA achieved a linear output power of 19 dBm, with a respective PAE of 29% at the 2.45 GHz operating frequency.

A.S. Rawat et al. (2022) presented a CMOS PA with adaptive bias technique for LORA application operating at 919–923 MHz [149]. The driver stage of the CMOS PA utilized a bias voltage modulation mechanism, while the main PA stage used a split bias mechanism to achieve different power level modes. A bias circuit controlled the channel current of the driver and the main PA via the applied gate voltage. The main PA was split into two units, in which each of them was adaptively biased to achieve the optimized linearity performance. A linear output power of 21 dBm, with a respective PAE of 29% at 920 MHz, was obtained. A. S. Rawat et al. (2023) also presented another CMOS PA with a switching mechanism for adaptive-device-sizing biasing [150]. This CMOS PA also employed a high Q-factor compact inductor for efficiency enhancement at linear output power. The adaptive device sizing was implemented to enable the low-power and high-power modes for the PA. The switching of the modes was selected through a NMOS pass transistor. Two individual bias circuits were utilized to conduct the adaptive biasing for the main PA stage. For the low-power mode, only one of the bias circuits was turned ON. In contrast, both bias circuits were turned ON for the high-power mode operation. Thus, the linear output power can be increased with minimum trade-off with efficiency via this method. The proposed CMOS PA achieved a linear output power of 21.5 dBm, with a respective PAE of 22%. Table 3 summarizes the recent state-of-the-art CMOS PAs with linearity enhancement techniques.

**Table 3.** Summary of the recent state-of-the-art CMOS PAs with linearity enhancement techniques.

Architecture	Year	Tech (nm)	V <sub>DD</sub> (V)	Freq. (GHz)	Linear. P <sub>out</sub> (dBm)	Linear PAE (%)	Ref.
Feedback/Feedforward	2016	130	1.2	0.868	10.4	29.0	[116] <sup>+</sup>
	2013	150	3.3	1.75	24.0	16.0	[118]
	2013	65	2.0	2.0	20.4	32.3	[119]
	2015	180	3.6	24.0	14.6	12.6	[121]
LINC	2010	180	3.3	1.95	26.0	20.0	[123]
	2013	130	3.5	1.95	28.5	29.6	[124]
Pre-Distortion	2012	180	3.5	1.95	29.1	41.1	[129]
	2018	45	4.8	15.0	20.6	21.8	[132]
	2021	180	3.3	0.8–3.3	20.0	34.0	[133]
	2021	180	3.3	0.4–2.8	21.0	34.6	[134]
	2021	180	3.3	1.7–2.7	25.0	38.0	[135]
	2023	180	3.3	1.7–2.7	25.1	38.8	[136]
	2023	180	3.3	5.3	21.0	6.0	[137]
	2014	180	3.5	1.7–2.0	28.0	42.0	[142]
	2017	28	3.3	2.4	26.8	21.2	[143]
Adaptive Biasing	2014	180	3.5	0.87	28.5	22.0	[144]
	2015	180	3.3	1.75	22.0	39.3	[145]
	2016	40	-	0.65	17.5	10.5	[146]
	2020	130	2.5	2.4	23.5	18.1	[147]
	2021	180	3.3	2.45	19.0	29.0	[148]
	2022	180	3.3	0.92	21.0	29.0	[149]
	2023	130	3.3	0.92	21.5	22.0	[150]

<sup>+</sup> simulated.

Figure 25 depicts the plot of the linear PAE across the achieved linear output power by the aforementioned linearization techniques. It can be observed that most of the employed techniques achieved a linear output power of more than 20 dBm. Most of the CMOS PAs that employ the analog predistortion technique were capable of achieving more than 30% linear PAE. Also, it can be deduced that the CMOS PAs were still limited in delivering a watt-level linear output power, since the PAs were required to operate at a backed-off output power to sustain the linear transmission.



The signal is amplified via its transconductance and accumulates along the drain line as the signal passes through the PA. The DA method produces a wide bandwidth as a result of the low-pass structures, which produce high cut-off frequencies. The impedance of the input line is defined as

$$Z_{og} = \left( \frac{L_g}{C_{ds}} \right)^2 \quad (19)$$

In contrast, the impedance of the drain line is defined as

$$Z_{od} = \left( \frac{L_d}{C_{ds}} \right)^{\frac{1}{2}} \quad (20)$$

Since the gate capacitance restricts the achievable bandwidth of the DA, the cut-off frequency is defined as

$$f_c = \frac{1}{\pi Z_{og} C_{gs}} \quad (21)$$

Figure 27 shows the frequency response comparison of a DA and PA with lumped elements.

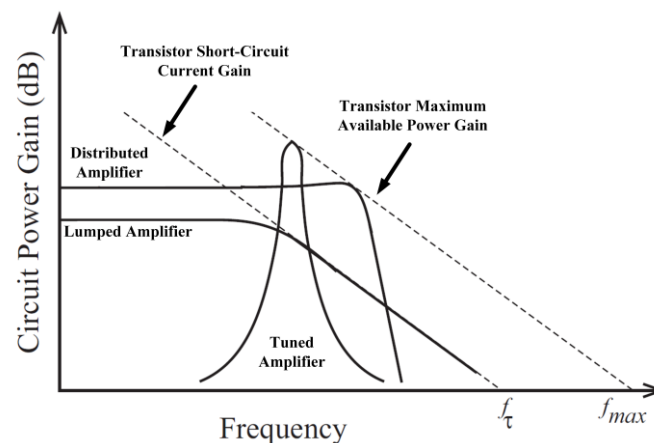


Figure 27. Frequency response comparison.

C. Hsiao et al. (2013) proposed a CMOS DA that employs a gate–drain transformer feedback method [154]. This employed feedback method permits the reuse of the traveling signal in order to attain a large gain bandwidth while preserving the low power consumption of the DA. The utilized transformer is miniaturized via a folded transmission lines configuration. A patterned ground shield (PGS) is employed to enhance the quality factor of the transformer. The transformer also has a well-controlled feedback coupling coefficient. This proposed DA achieved a 3 dB bandwidth of 61.3 GHz, with power consumption under 60 mW.

Furthermore, P. Chen et al. (2014) presented a DC–80 GHz compact CMOS DA based on a conventional DA with the gain cell of a cascaded single-stage DA (CSSDA) [155]. To make it area efficient, the artificial transmission lines (ATL) were employed with a micro-strip line instead of a coplanar waveguide. The inter-digital capacitors utilized in this design were optimized for wideband frequency response. The achieved 3 dB bandwidth was 80 GHz, with power consumption under 90 mW.

Y. Zhang et al. (2017) proposed a CMOS DA comprised of two three-stage DAs integrated with an input ATL that served as a preamplifier for broadband impedance matching as well as gain enhancement [156]. In addition, two four-stage DAs were integrated with the output ATLs that served as a medium PA to exhibit the high output power for a wide bandwidth. This proposed DA had a bandwidth operation from 2 to 22 GHz.

M. M. Tarar et al. (2017) presented a wideband stacked distributed CMOS PA [157]. A four-transistor stack was employed to achieve a high output swing and gain. Voltage

alignment was achieved by allowing a small AC swing at the gate to be derived from the voltage division between  $C_{gs}$  and the external gate capacitance. The four-transistor stack was replicated in the distributed configuration, which contributed to the wideband operation. This PA was capable of operating with a bandwidth from 2 to 16 GHz.

### 5.2. Cascode Technique

A cascode configuration is employed by connecting common-source (CS) and common-gate (CG) transistors in series, as illustrated in Figure 28. The cascode topology is widely utilized in PA designs to enhance the gain and bandwidth [158]. The cascode structure has several advantages, which include high output impedance, high reverse isolation, and less sensitivity to the output resistance of the transistors. High reverse isolation is contributed to by the low Miller feedback capacitance. Moreover, the reduction in Miller capacitance exhibits a 3–4 dB higher gain and increased bandwidth compared to CS structures [159].

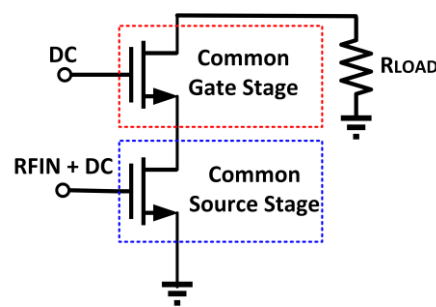


Figure 28. Cascode PA configuration.

In a CS configured device, the reduction in the Miller capacitance in the gate–drain parasitic capacitance ( $C_{gd}$ ) generates a frequency pole that makes a small signal gain roll down. The Miller capacitance in the  $C_{gd}$  for a CS amplifier with a voltage gain of  $A_v = -g_m R_{load}$  is given by

$$C_M = C_{gd}(1 + A_v) \quad (22)$$

The increase in Miller capacitance reduces the bandwidth of the PA. When the cascode transistor is integrated as a load to the drain of the CS amplifier, the Miller effect is eliminated regardless of the load impedance. This feature enhances the bandwidth of the PA. In a two-identical-cascodes device, the small signal open loop voltage gain is defined as [160]

$$A_{vo} = \frac{v_o}{v_i} = -g_{m1}r_{o1}x(1 + g_{m2}r_{o2}) \approx -g_{m1}r_{o1}g_{m2}r_{o2} \approx -g_m^2r_o^2 \quad (23)$$

where  $g_m$  is the small signal transconductance gain, and  $r_o$  is the transistor output impedance. S. Leuschner et al. (2011) proposed a multi-band CMOS PA with a cascode configuration output stage for WCDMA application [161]. A two-stage interstage matching network was utilized to achieve a wideband operation of more than 300 MHz. The cascode PA achieved an efficiency of more than 45% across the operating bandwidth. H. Jeon et al. (2013) proposed a CMOS multi-stage cascode PA with a feedback bias technique [162]. The feedback bias technique was utilized to enhance the linearity and reliability across a wideband frequency range. By utilizing the large parasitic capacitance and low substrate resistivity of the CMOS process, the signal swings were coupled between the ports of the transistors. The leakage signals at the gate of CG structure were employed for the negative feedback. The proposed cascode PA achieved a 3 dB bandwidth of 1.5–2.1 GHz.

H. Wu et al. (2016) proposed a two-stage three-stacked PA with a wideband gain [163]. Wideband load impedance matching was achieved by utilizing modified stacked field-effect transistors with a resistive feedback. To realize the wideband gain frequency response, the compensation between the driver amplifier's expanding gain response and the last-stage amplifier's compressing gain response was utilized. The PA achieved a bandwidth of 6.4 GHz from 0.1 to 6.5 GHz. It delivered a maximum output power of 22–24.3 dBm,

with a peak efficiency of 13–20%. The achieved efficiency was quite low due to the three-stacked FETs employed at the driver and the last stages, which consume 39.1% and 41% of power, respectively.

In addition, S. Kang et al. (2018) presented a cascode CMOS PA with integrated dynamic body linearizers [164]. The dynamic body linearizers were employed based on the envelope signal injection to the bulk of the CS and CG configured transistors. The dynamic body linearizers mitigated the parasitic capacitances, and these capacitances could limit the modulation bandwidth due to the delays cause by them between the dynamic bias linearizer’s output and the input envelope signals. This cascode PA was capable of performing from 1.7 to 2.0 GHz.

T. Guo et al. (2022) proposed a cascode CMOS PA with a split push–pull configuration at both the driver and main PA stages [165]. This CMOS PA also employed floating-body transistors in both stages. An on-chip bandgap voltage reference was implemented in the design in which it generated the temperature-independent biasing voltage for both the driver and main PA. The design also utilized on-chip transformer baluns for power splitting and combining. The baluns also acted as the wideband impedance matching for the input and output of the CMOS PA. This proposed CMOS PA achieved an operating frequency bandwidth of 4.3–6.4 GHz. This PA achieved a maximum output of 22.2 dBm at 4.9 GHz and a peak PAE of 28% at 4.7 GHz.

### 5.3. Shunt Feedback Technique

Resistive shunt feedback is a common technique employed to provide wideband matching in PAs. A PA with a resistive feedback provides a good output reflection coefficient. The common practice is to implement a negative resistor feedback from the drain to the gate, as depicted in Figure 29 [166].

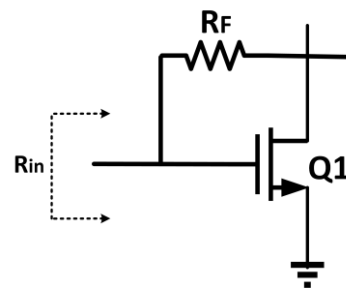


Figure 29. Configuration of a resistive feedback.

Referring to Figure 29, for a PA with a gain of  $A_v$ , the input resistance,  $R_{in}$ , is given by

$$R_{in} = \frac{R_F}{1 + A_v} \tag{24}$$

A small  $R_F$  provides excellent matching but with the cost of a reduced gain due to the signal feedback through this path. Contrarily, a large  $R_F$  provides a high gain but reduces the effect of the feedback.

A straightforward feedback resistor is not adequate when the bandwidth requirements are very large. Thus, some combination of passive or active elements is required in the feedback path. Considering a feedback employed in a CS configured amplifier, a small signal model is shown in Figure 30. Based on Figure 30, the input impedance of a CS configured amplifier is given as

$$Z'_{in} = sL_{bond} + \frac{1}{sC_{gs}} + \frac{g_m L_{bond}}{C_{gs} + C_{gd}} \tag{25}$$

$$g_{m,eff} = \frac{g_m v_{gs}}{v_{in}} = \frac{g_m}{1 + s g_m L_{bond}} \tag{26}$$

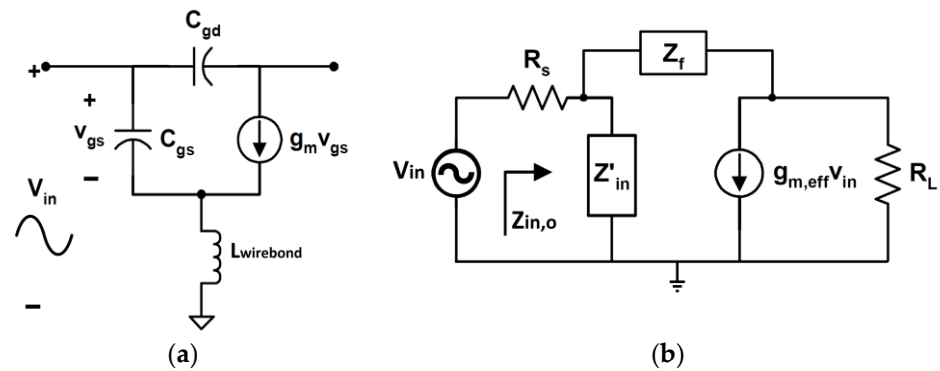


Figure 30. (a) Small signal model of CS; (b) small signal model of CS with feedback.

After employing a feedback into the CS amplifier, the input and output impedances and their corresponding gains are defined as

$$Z_{in,o} = \frac{Z'_{in} Z_f}{Z_f + (A_v - 1) Z'_{in}} \tag{27}$$

$$Z_{out,o} = \frac{Z_f (R_s \parallel Z'_{in})}{1 + g_{m,eff} (R_s \parallel Z'_{in})} \tag{28}$$

$$A_v = \frac{R_L + g_{m,eff} Z_f R_L}{R_L - Z_f} \tag{29}$$

Since  $Z'_{in}$  and  $g_{m,eff}$  are frequency-dependent parameters, the characteristics of  $Z_f$  also correspondingly vary across the frequency band.

S. A. Z. Murad et al. (2010) presented a CMOS PA with a resistive feedback to achieve a wideband flat gain [167]. This PA also adopted a cascode topology with a current reuse method that was utilized to increase the gain at the upper end of the operating band. An inter-stage inductor was employed in between the first and second stages of the PA, which further contributed to the gain flatness. This proposed PA achieved a flat gain with  $\pm 0.8$  dB deviation from 3.1 to 4.8 GHz and a 3 dB bandwidth of 2.8–5.0 GHz.

S. A. Z. Murad et al. (2010) also presented a wideband CMOS PA, which achieved a flat gain by employing a shunt–shunt feedback [168]. This PA utilized a current reuse technique in the first stage to enhance the gain at the upper band of the operating frequency. The second stage of the PA consisted of a shunt and series peaking inductors with a resistive feedback and a shunt–shunt feedback. The resonance circuit in this PA provided a narrow band characteristic that increased the gain at the upper end of the operating frequency (7 GHz). A shunt inductor was inductively peaking at the low frequency region (3 GHz), thus realizing a wide-bandwidth gain. A series peaking inductor was employed between the first and second stages in order to increase the middle band’s gain. This contributed to the gain flatness across the wide bandwidth. The employed resistive feedback aided in further flattening the gain. A shunt–shunt feedback using a resistor and a capacitor further increased the bandwidth and improved the wideband output matching. This PA achieved a flat gain with  $\pm 0.5$  dB deviation from 3.0 to 7.0 GHz as well as a 3 dB bandwidth of 2.8–7.4 GHz.

In addition, N. Ginzberg et al. (2023) presented a wideband CMOS PA that implemented a cascode topology with a resistive shunt–shunt feedback [169]. This CMOS PA was biased in the class B operation region. The design adopted simultaneous input and output matching via the feedback resistor. The biasing network was also resistively implemented in order to achieve a wideband response. The shunt–shunt resistive feedback technique was required to conduct impedance matching as well as stability. In order to achieve both unconditional stability and optimum input matching, a 15  $\Omega$  resistor was employed

at the input. This proposed CMOS PA achieved an operating frequency bandwidth of 0.33–2.5 GHz. The maximum output power delivered was 21.5 dBm, with a peak PAE of 52.4% at 1 GHz.

#### 5.4. Switched Capacitor Technique

A switched capacitor PA (SCPA) has been extensively trending in recent years, and it employs an array of capacitors that are tuned between the supply and ground [170–177]. Figure 31 shows the schematic of the basic switched capacitor (SC) architecture [178].

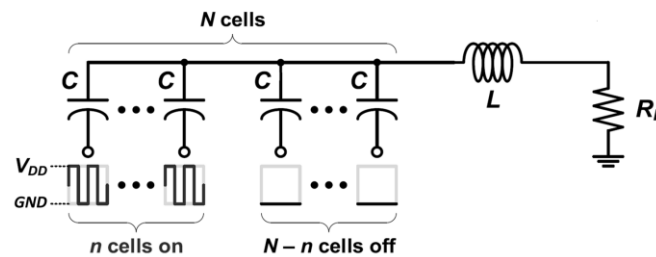


Figure 31. Schematic of the basic switched capacitor (SC) architecture.

The amplitude of the signal is created by a capacitive voltage division between the switched-on capacitors and switched-off capacitors as follows [179]:

$$V_{out} = \frac{C_{ON}}{C_{ON} + C_{OFF}} \cdot V_{DD} = \frac{C_{ON}}{C} \cdot V_{DD} \quad (30)$$

where  $C_{ON}$  is the equivalent capacitance of the switched-on capacitors,  $C_{OFF}$  is the equivalent capacitance of the switched-off capacitors, and  $C$  is the total array capacitance. The capacitor array is integrated with a band-pass matching network that resonates the total capacitance at the frequency of application.

The output power is obtained by considering the output voltage as a fundamental component of the Fourier-series expansion of a square wave signal. The output voltage and power are given as

$$V_{out} = \left(\frac{2}{\pi}\right) \left(\frac{n}{N}\right) V_{DD} \quad (31)$$

$$P_{out} = \left(\frac{2}{\pi^2}\right) \left(\frac{n}{N}\right)^2 \frac{V_{DD}^2}{R_{opt}} \quad (32)$$

where  $n$  is the number of switched-on capacitors, and  $N$  is the total capacitance. The PAE of the SCPA is given by

$$PAE = \frac{P_{out}}{P_{DC,SCPA} + P_{SW,in}} \quad (33)$$

where  $P_{SW,in}$  is the dynamic losses of the SCPA core drivers and the clock distribution network, and  $P_{DC,SCPA}$  is the average power consumption of the PA core.  $P_{DC,SCPA}$  also takes into account the ohmic losses of the switch resistances as well as the dynamic power required for the charging and discharging of the capacitor array [180].

S. Goswami et al. (2014) presented a CMOS PA with a frequency agile solution that was tunable over a wide-bandwidth frequency [181]. This CMOS PA utilized a class D configured out-phasing technique with an integrated tunable matching network. The tunable matching network was realized via a series combining a transformer and a digitally tuned capacitor bank. The unit capacitance was employed in unary weighted mode. The proposed PA was implemented using 45 nm CMOS SOI technology with a supply headroom of 1.8 V. It was capable of operating from 1.44 to 3.41 GHz, with a bandwidth of 1.97 GHz. This PA delivered a maximum output power of 27–28.2 dBm across the frequency, with a peak efficiency of 25–30%. The achieved linear output power was 21.6–23.4 dBm, with an efficiency of 9.8–17.4% across the frequency of operation.

S. Yoo et al. (2011) presented an SCPA for EER or polar transmitters without the need for a supply modulator [182]. A baseband DSP was employed to generate a polar-modulated signal, and the number of capacitors to be switched were controlled by the digital envelope input signal to a thermometer decoder. This SCPA can be considered as a capacitive power combination of multiple switching PAs in which the output power is the combination of the charge redistribution on the capacitors. This proposed PA was capable of operating from 1.8 to 2.8 GHz.

Furthermore, W. Yuan et al. (2016) proposed a digital-based class G quadrature SCPA, which combined the I and Q signals on a shared capacitor array [183]. This proposed Q-SCPA did not need a wideband phase modulator or a delay matching circuitry, unlike its polar or EER counterparts. The capacitor array was subdivided in such a way that half of the array was located in the path of the individual 1/Q paths. The subarrays were also divided into unit capacitors. The unit capacitors had individual driver chains that could be switched on and off. A 3 dB bandwidth of 400 MHz from 1.9 to 2.3 GHz was achieved by the proposed SCPA.

Z. Bai et al. (2018) proposed a multiphase SCPA consisting of C-2C split array capacitors [184]. This SCPA was designed for 16-bit resolution for additional linearization or calibration states using DPD. C-2C arrays are extensively utilized due to the low ratio of the maximum capacitance to the minimum capacitance, which offers a better impedance matching [185,186]. However, this comes with the expense of increased sensitivity to parasitic effects [187,188]. The C-2C method consumes less area compared to binary weight arrays because C-2C arrays linearly increase with the resolution. The proposed SCPA achieved a 3 dB bandwidth of 700 MHz from a center frequency of 1.8 GHz. Moreover, Z. Bai et al. (2019) also presented a frequency-tunable SCPA that achieved an operating bandwidth of more than 1 GHz [189]. This SCPA was employed in series with an inductor and a digitally programmable capacitor (DPC). The frequency tuning of the SCPA resonance was conducted by the DPC. The SCPA comprised an 8-bit array that consisted of 4-unary and 4-binary weighted bits. The switch and driver stages were employed as custom cells that can be tiled with nearby cells in order to mitigate parasitic capacitance. This proposed SCPA was capable of tuning its frequency from 1.4 to 2.5 GHz of bandwidth, while maintaining an output power of 20–21.7 dBm.

I. Raja et al. (2020) proposed a reconfigurable RF transmitter with an integrated tunable class E PA [190]. A DSP was utilized to minimize the sampling spurs up to the harmonics of the carrier, which avoided the requirement for sharp RF filters. Other than that, a DPD was also employed as a linearizer for the class E PA. Clock correction circuitry was implemented for rectifying the duty cycle and quadrature errors. In the impedance matching network, the capacitors were made tunable to provide wave shaping across the frequency range, while using a single, fixed-series inductor. The switching transistors were the control bits for the tunable capacitor bank. The capacitors were segmented into smaller capacitors in order to achieve an effective tuning. This proposed PA had a bandwidth of 1.75 GHz, from 0.75 to 2.5 GHz. This PA delivered a maximum linear output power of 6.5–13.0 dBm, with a linear efficiency of 5–27%, when tested with a 25-kS/s 16-QAM signal. In addition, the finite impulse response (FIR) filters, DPD segments, and the RF choke inductor were employed off-chip in this design. Table 4 summarizes the recent state-of-the-art CMOS PAs with bandwidth enhancement techniques.

Figure 32 shows the summary of the frequency bandwidths achieved by the proposed bandwidth enhancement techniques. Based on Figure 32, the largest bandwidth is achieved by the distributed technique, which has a range from the DC level to 80 GHz. However, the other performance parameters of the PA such as its output power and PAE are very low for this technique. The other techniques are capable of achieving an operating bandwidth of more than 1 GHz, with an optimum output power and PAE for its given application. The switched-capacitor-based CMOS PA has the most flexibility and configurability in tuning its parameters according to its need, since its impedance can be varied.

**Table 4.** Summary of the recent state-of-the-art CMOS PAs with bandwidth enhancement techniques.

Architecture	Year	Tech (nm)	V <sub>DD</sub> (V)	Freq. (GHz)	Bandwidth (GHz)	Ref.
Distributed	2013	90	2.2	DC–61.3	61.3	[154]
	2014	40	1.7	DC–80.0	80.0	[155]
	2017	180	2.8	1.0–23.8	22.8	[156]
	2017	130	3.5	2.0–16.0	14.0	[157]
Cascode	2011	65	3.4	1.64–1.95	0.31	[161]
	2013	180	3.4	1.5–2.1	0.6	[162]
	2016	180	6.0	0.1–6.5	6.4	[163]
	2018	180	3.3	1.7–2.0	0.3	[164]
	2022	130	3.3	4.3–6.4	2.1	[165]
Shunt Feedback	2010	180	1.8	2.6–5.0	2.4	[167]
	2010	180	1.8	3.0–7.0	4.0	[168]
	2023	65	3.3	0.33–2.5	2.17	[169]
Adaptive Biasing	2014	45	2.0	1.3–3.3	2.0	[181]
	2011	90	2.5	1.8–2.8	1.0	[182]
	2016	65	2.4	1.8–2.3	0.5	[183]
	2018	65	2.4	1.4–2.1	0.7	[184]
	2019	65	2.4	1.4–2.5	0.9	[189]
2020	130	1.5	0.75–2.5	1.75	[190]	

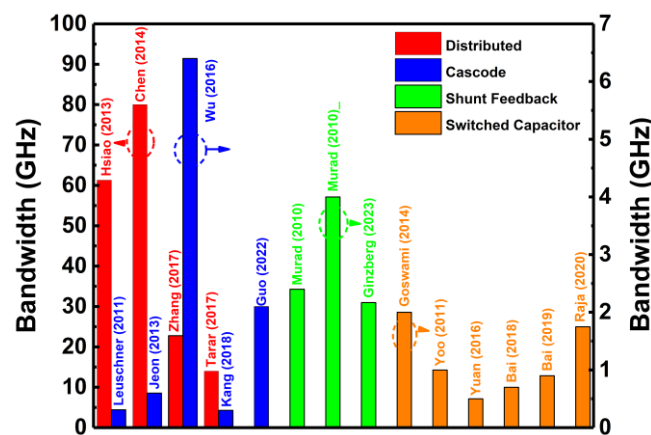


**Figure 32.** Frequency bandwidth achieved by the proposed bandwidth enhancement techniques [154–157,161–165,167–169,181–184,189,190].

### 6. Conclusions

This review paper discusses the trending state-of-the-art CMOS RFPAs in wireless communication systems. As the number of wireless devices and mobile data usage increase, there is a growing need for enhancements and upgrades to current wireless communication systems. This review provides a concise discussion of the performance metrics that are important for designing a CMOS PA, followed by an overview of recent research on CMOS PAs’ performance enhancement techniques, including efficiency, linearity, and bandwidth. This review concludes that there is a trade-off between efficiency, linearity, and bandwidth in CMOS PAs, and several enhancement techniques are developed to improve their performance. The on-chip transformer and out-phasing techniques are capable of delivering watt-level maximum output power for CMOS PAs. This is due to the usage of power-combining architectures in these techniques that boost the maximum output power. It can also be deduced that CMOS PAs are still limited in delivering watt-level linear output power, since PAs are required to operate at backed-off output power to sustain the linear transmission. The switched-capacitor-based CMOS PA has the most flexibility and configurability in tuning its parameters according to its need, since its impedance can be tuned.

**Author Contributions:** Conceptualization, S.S.H., S.M., J.R. and B.S.Y.; methodology, S.S.H., S.M. and J.R.; software, S.M. and J.R.; formal analysis, S.M., J.R., N.K., N.A.R. and A.N.; validation, S.M., J.R., N.K., A.N. and B.S.Y.; resources, S.S.H., J.R., S.M., A.S.R. and N.K.; data curation, J.R., S.M., N.A.R. and A.N.; writing—original draft preparation, S.S.H., J.R., S.M. and N.K.; writing—review and editing, J.R., S.M., N.K. and A.N.; visualization, S.M., N.A.R., A.S.R. and N.K.; supervision, J.R. and A.N.; project administration, J.R. and S.M.; funding acquisition, J.R. and S.M. All authors have read and agreed to the published version of the manuscript.

**Funding:** The Malaysian Ministry of Higher Education’s Fundamental Research Grant Scheme (grant number: FRGS/1/2019/TK04/USM/02/14).

**Data Availability Statement:** Not applicable.

**Conflicts of Interest:** The authors declare no conflict of interest.

## References

1. Ericsson. Ericsson Mobility Report June 2016. 2016. Available online: <https://www.ericsson.com/res/docs/2016/ericsson-mobility-report-2016.pdf> (accessed on 12 April 2023).
2. Lie, D.Y.C. RF-SoC’: Integration trends of on-chip CMOS power amplifier: Benefits of external PA versus integrated PA for portable wireless communications. *Int. J. Microw. Sci. Technol.* **2010**, *380108*. [[CrossRef](#)]
3. Bennett, H.S.; Brederlow, R.; Costa, J.C.; Cottrell, P.E.; Huang, W.M.; Immorlica, A.A.; Mueller, J.E.; Racanelli, M.; Shichijo, H.; Weitzal, C.E.; et al. Device and technology evolution for Si-based RF integrated circuits. *IEEE Trans. Electron Devices* **2005**, *52*, 1235–1258. [[CrossRef](#)]
4. Larson, L.E. Silicon technology tradeoffs for radio-frequency/mixed-signal ‘systems-on-a-chip’. *IEEE Trans. Electron Devices* **2003**, *50*, 683–699. [[CrossRef](#)]
5. Chang, C.S.; Chao, C.P.; Chern, J.G.J.; Sun, J.Y. Advanced CMOS technology portfolio for RF IC applications. *IEEE Trans. Electron Devices* **2005**, *52*, 1324–1334. [[CrossRef](#)]
6. Abidi, A.A. RF CMOS comes of age. *IEEE J. Solid-State Circuits* **2004**, *39*, 549–561. [[CrossRef](#)]
7. Hajimiri, A. Fully integrated RF CMOS power amplifiers—A prelude to full radio integration. In Proceedings of the 2005 IEEE Radio Frequency Integrated Circuits (RFIC) Symposium—Digest of Papers, Long Beach, CA, USA, 12–14 June 2005; pp. 439–442. [[CrossRef](#)]
8. Hajimiri, A. Next-Generation CMOS RF Power Amplifiers. *IEEE Microw. Mag.* **2011**, *12*, 38–45. [[CrossRef](#)]
9. Niknejad, A.A.M.; Chowdhury, D.; Chen, J. Design of CMOS Power Amplifiers. *IEEE Trans. Microw. Theory Tech.* **2012**, *60*, 1784–1796. [[CrossRef](#)]
10. Nobbe, D.W. Silicon technology status and perspectives for multi-band and multi-standard challenges in upcoming RF frontends. In Proceedings of the 2008 IEEE Radio and Wireless Symposium, Orlando, FL, USA, 22–24 January 2008; pp. 191–194. [[CrossRef](#)]
11. Kang, D.; Park, B.; Kim, D.; Kim, J.; Cho, Y.; Kim, B. Envelope-Tracking CMOS Power Amplifier Module for LTE Applications. *IEEE Trans. Microw. Theory Tech.* **2013**, *61*, 3763–3773. [[CrossRef](#)]
12. Mariappan, S.; Rajendran, J.; Noh, N.M.; Ramiah, H. A 29dBm OIP3 Dual-Stage Power Amplifier with Analog Pre-Distorter in 0.18 $\mu$ m CMOS for IoT Transceiver. *IETE J. Res.* **2019**, *68*, 2298–2304. [[CrossRef](#)]
13. Mariappan, S.; Rajendran, J.; Noh, N.M.; Ramiah, H. Low voltage CMOS power amplifier with integrated analog Pre-Distorter for BLE 4.0 application. *Indonesian J. Electr. Eng. Comput.* **2019**, *14*, 895–902. [[CrossRef](#)]
14. Mariappan, S.; Rajendran, J.; Noh, N.M.; Ramiah, H.; Manaf, A.A. Energy efficiency in CMOS power amplifier designs for ultra-low power mobile wireless communication systems. *Turk. J. Electr. Eng. Comput. Sci.* **2020**, *28*, 1–16. [[CrossRef](#)]
15. Mariappan, S.; Rajendran, J.; Noh, N.M.; Ramiah, H.; Manaf, A.A. The Evolution of Integrated CMOS Power Amplifiers for Next Generation Mobile Wireless Transceivers. *J. Circuits Syst. Comput* **2019**, *29*, 2030007. [[CrossRef](#)]
16. Johansson, T.; Fritzin, J. A Review of Watt-Level CMOS RF Power Amplifiers. *IEEE Trans. Microw. Theory Tech.* **2014**, *62*, 111–124. [[CrossRef](#)]
17. Eswaran, U.; Ramiah, H.; Kanesan, J.; Reza, A.W. Energy saving power amplifier design methodologies for mobile wireless communications. *Renew. Sustain. Energy Rev.* **2015**, *51*, 1721–1727. [[CrossRef](#)]
18. Gunasegaran, P.; Rajendran, J.; Mariappan, S.; Yusof, Y.M.; Aziz, Z.A.A.; Kumar, N. A fully matched dual stage CMOS power amplifier with integrated passive linearizer attaining 23 dB gain, 40% PAE and 28 dBm OIP3. *Microelectron. Int.* **2021**, *38*, 66–77. [[CrossRef](#)]
19. Sapawi, R.; Mohamad, D.H.A.; Yusof, D.S.A.A.; Sahari, S.K.; Salleh, D.N.S.D.A.; Hazis, N.A.H.A.; Murad, S.A.Z. CMOS Power Amplifier Design Techniques for UWB Communication: A Review. *J. Telecommun. Electron. Comput. Eng.* **2017**, *9*, 1–8.
20. Yin, Y.; Chi, B.; Xia, Z.; Wang, Z. A Reconfigurable Dual-Mode CMOS Power Amplifier with Integrated T/R Switch for 0.1–1.5 GHz Multistandard Applications. *IEEE Trans. Circuits Syst. II Express Briefs* **2014**, *61*, 471–475. [[CrossRef](#)]
21. Shim, S.; Han, J.; Hong, S. A CMOS RF Polar Transmitter of a UHF Mobile RFID Reader for High Power Efficiency. *IEEE Microw. Wirel. Compon. Lett.* **2008**, *18*, 635–637. [[CrossRef](#)]

22. Quinlan, P.; Crowley, P.; Chanca, M.; Hudson, S.; Hunt, B.; Mulvaney, K.; Reta, G.; O'Sullivan, C.E.; Walsh, P. A multimode 0.3–200-kb/s transceiver for the 433/868/915-MHz bands in 0.25- $\mu\text{m}$  CMOS. *IEEE J. Solid-State Circuits* **2004**, *39*, 2297–2310. [[CrossRef](#)]
23. Osseiran, A.; Monserrat, J.F.; Marsch, P. *5G Mobile and Wireless Communications Technology*; Cambridge University Press: Cambridge, UK, 2016.
24. Walsh, K.; Johnson, J. 3G/4G Multimode Cellular Front-End Challenges; Impact on Power Amplifier Design. *Microw. J.* **2009**, *3*, 56–68.
25. *Specification of the Bluetooth System—'Bluetooth Specification Version 2.0 + EDR'*; 2004; Volume 3, p. 31. Available online: <https://www.bluetooth.com/specifications/specs/core-specification-2-0-edr/> (accessed on 28 July 2023).
26. Miller, M. *Discovering Bluetooth*; SYBEX: Alameda, CA, USA, 2001.
27. Skaria, G. Class F and Inverse Class F Power Amplifier Subject to Electrical Stress Effect. Master's Thesis, University of Central Florida, Orlando, FL, USA, 2011.
28. Anakabe, A.; Ayllón, N.; Collantes, J.M.; Mallet, A.; Soubercaze-Pun, G.; Narendra, K. Automatic pole-zero identification for multivariable large-signal stability analysis of RF and microwave circuits. In Proceedings of the 40th European Microwave Conference, Paris, France, 28–30 September 2010; pp. 477–480.
29. Dellier, S.; Gourseyrol, R.; Soubercaze-Pun, G.; Collantes, J.; Anakabe, A.; Narendra, K. Stability analysis of microwave circuits. In Proceedings of the WAMICON 2012 IEEE Wireless & Microwave Technology Conference, Cocoa Beach, FL, USA, 15–17 April 2012; pp. 1–5.
30. Narendra, K.; Limiti, E.; Paoloni, C.; Collantes, J.; Jansen, R.; Yarman, S. Vectorially Combined Distributed Power Amplifiers for Software-Defined Radio Applications. *IEEE Trans. Microwave Theory Tech.* **2012**, *60*, 3189–3200. [[CrossRef](#)]
31. Imbornone, J.F.; Murphy, M.T.; Donahue, R.S.; Heaney, E. New insight into subharmonic oscillation mode of GaAs power amplifiers under severe output mismatch condition. *IEEE J. Solid-State Circuits* **1997**, *32*, 1319–1325. [[CrossRef](#)]
32. Qiao, D.; Zhao, Y.; Hung, T.; Kimball, D.; Li, M.; Asbeck, P.; Choi, D.; Kelly, D. Antenna impedance mismatch measurement and correction for adaptive CDMA transceivers. In Proceedings of the IEEE MTT-S International Microwave Symposium Digest, Long Beach, CA, USA, 17 June 2005.
33. Van Bezooijen, A.; Chanlo, C.; Van Roermund, A.H.M. Adaptively preserving power amplifier linearity under antenna mismatch. In Proceedings of the 2004 IEEE MTT-S International Microwave Symposium Digest (IEEE Cat. No. 04CH37535), Fort Worth, TX, USA, 6–11 June 2004; Volume 3, pp. 1515–1518.
34. Keerti, A.; Pham, A.H. RF Characterization of SiGe HBT Power Amplifiers Under Load Mismatch. *IEEE Trans. Microw. Theory Tech.* **2007**, *55*, 207–214. [[CrossRef](#)]
35. Karoui, W.; Parra, T. A protection circuit for HBT RF Power Amplifier under load mismatch conditions. In Proceedings of the 2008 Joint 6th International IEEE Northeast Workshop on Circuits and Systems and TAISA Conference, Montreal, QC, Canada, 22–25 June 2008; pp. 241–244. [[CrossRef](#)]
36. Suárez, A.; Ramírez, F.; Sancho, S. Stability Analysis of Power Amplifiers Under Output Mismatch Effects. *IEEE Trans. Microw. Theory Tech.* **2014**, *62*, 2273–2289. [[CrossRef](#)]
37. De Vreede, L.C.N.; van der Heijden, M.P. Linearization Techniques at the Device and Circuit Level (Invited). In Proceedings of the 2006 Bipolar/BiCMOS Circuits and Technology Meeting, Maastricht, The Netherlands, 8–10 October 2006; pp. 1–8.
38. Texas Instrument. Intermodulation Distortion (IMD). Available online: <http://www.ti.com> (accessed on 16 May 2023).
39. Aitchison, C.S.; Mbabele, M. Third Order Intermodulation Improvement in Distributed Amplifiers. In Proceedings of the 31st European Microwave Conference, London, UK, 24–28 September 2001; pp. 1–4. [[CrossRef](#)]
40. Minasian, R.A. Intermodulation Distortion Analysis of MESFET Amplifiers Using the Volterra Series Representation. *IEEE Trans. Microw. Theory Tech.* **1980**, *28*, 1–8. [[CrossRef](#)]
41. Asbeck, P. Linearisation of RF Power Amplifiers. Ph.D. Thesis, Nokia Mobile Phones and Department of Information Technology, Technical University of Denmark, Lyngby, Denmark, 2001.
42. Aslan, M.P. Adaptive Digital Predistortion for Power Amplifier Linearization. Master's Thesis, The Institute of Engineering and Science of Bilkent University, Ankara, Turkey, 2008.
43. El-Khatib, Z. Highly-Linearized CMOS Distributed Bidirectional Amplifier with Cross-Coupled Compensator for Wireless Communications. Ph.D. Thesis, Ottawa-Carleton Institute for Electrical Engineering, Carleton University, Ottawa, ON, Canada, 2012.
44. Liu, C.; Xiao, H.; Wu, Q.; Li, F. Spectrum design of RF power amplifier for wireless communication systems. *IEEE Trans. Consum. Electron* **2002**, *48*, 72–80. [[CrossRef](#)]
45. Boulejfen, N.; Harguem, A.; Hammi, O.; Ghannouchi, F.M.; Gharsallah, A. Analytical prediction of spectral regrowth and correlated and uncorrelated distortion in multicarrier wireless transmitters exhibiting memory effects. *IET Microw. Antennas Propag.* **2010**, *4*, 685–696. [[CrossRef](#)]
46. Zhou, G.T.; Kenney, J.S. Predicting spectral regrowth of nonlinear power amplifiers. *IEEE Trans. Commun.* **2002**, *50*, 718–722. [[CrossRef](#)]
47. Nader, C.; Händel, P.; Björnsell, N. Peak-to-Average Power Reduction of OFDM Signals by Convex Optimization: Experimental Validation and Performance Optimization. *IEEE Trans. Instrum. Meas.* **2011**, *60*, 473–479. [[CrossRef](#)]

48. Ciccognani, W.; Colantonio, P.; Giannini, F.; Limiti, E.; Rossi, M. AM/AM and AM/PM power amplifier characterisation technique. In Proceedings of the 15th International Conference on Microwaves, Radar and Wireless Communications, Warsaw, Poland, 17–19 May 2004; pp. 678–681.
49. Katz, A. Linearization: Reducing distortion in power amplifiers. *IEEE Microw. Mag.* **2001**, *2*, 37–49. [[CrossRef](#)]
50. An, K.H.; Lee, O.; Kim, H.; Lee, D.H.; Han, J.; Yang, K.S.; Kim, Y.; Chang, J.J.; Woo, W.; Lee, C.-H. Power-Combining Transformer Techniques for Fully-Integrated CMOS Power Amplifiers. *IEEE J. Solid-State Circuits* **2008**, *43*, 1064–1075. [[CrossRef](#)]
51. Haldi, P.; Chowdhury, D.; Reynaert, P.; Liu, G.; Niknejad, A.M. A 5.8 GHz 1 V Linear Power Amplifier Using a Novel On-Chip Transformer Power Combiner in Standard 90 nm CMOS. *IEEE J. Solid-State Circuits* **2008**, *43*, 1054–1063. [[CrossRef](#)]
52. Chowdhury, D.; Hull, C.D.; Degani, O.B.; Wang, Y.; Niknejad, A.M. A Fully Integrated Dual-Mode Highly Linear 2.4 GHz CMOS Power Amplifier for 4G WiMax Applications. *IEEE J. Solid-State Circuits* **2009**, *44*, 3393–3402. [[CrossRef](#)]
53. Aoki, I.; Kee, S.D.; Rutledge, D.; Hajimiri, A. A 2.4-GHz, 2.2-W, 2-V fully-integrated CMOS circular-geometry active-transformer power amplifier. In Proceedings of the IEEE 2001 Custom Integrated Circuits Conference, San Diego, CA, USA, 9 May 2001; pp. 57–60. [[CrossRef](#)]
54. Aoki, I.; Kee, S.D.; Rutledge, D.B.; Hajimiri, A. Distributed active transformer—a new power-combining and impedance-transformation technique. *IEEE Trans. Microw. Theory Tech* **2002**, *50*, 316–331. [[CrossRef](#)]
55. Javidan, J.; Atarodi, M.; Luong, H.C. High Power Amplifier Based on a Transformer-Type Power Combiner in CMOS Technology. *IEEE Trans. Circuits Syst. II* **2010**, *57*, 838–842. [[CrossRef](#)]
56. Liu, G.; Liu, T.K.; Niknejad, A.M. A 1.2V, 2.4 GHz Fully Integrated Linear CMOS Power Amplifier with Efficiency Enhancement. In Proceedings of the IEEE Custom Integrated Circuits Conference 2006, San Jose, CA, USA, 10–13 September 2006; pp. 141–144. [[CrossRef](#)]
57. Liu, G.; Haldi, P.; Liu TJ, K.; Niknejad, A.M. Fully Integrated CMOS Power Amplifier with Efficiency Enhancement at Power Back-Off. *IEEE J. Solid-State Circuits* **2008**, *43*, 600–609. [[CrossRef](#)]
58. Afsahi, A.; Larson, L.E. An integrated 33.5 dBm linear 2.4 GHz power amplifier in 65nm CMOS for WLAN applications. In Proceedings of the IEEE Custom Integrated Circuits Conference 2010, San Jose, CA, USA, 19–22 September 2010; pp. 1–4. [[CrossRef](#)]
59. An, K.H.; Kim, Y.; Lee, O.; Yang, K.S.; Kim, H.; Woo, W.; Chang, J.J.; Lee, C.-H.; Kim, H.; Laskar, J. A Monolithic Voltage-Boosting Parallel-Primary Transformer Structures for Fully Integrated CMOS Power Amplifier Design. In Proceedings of the 2007 IEEE Radio Frequency Integrated Circuits (RFIC) Symposium, Honolulu, HI, USA, 3–5 June 2007; pp. 419–422. [[CrossRef](#)]
60. Belabad, A.R.; Masoumi, N.; Ashtiani, S.J. A fully integrated 2.4 GHz CMOS high power amplifier using parallel class A & B power amplifier and power-combining transformer for WiMAX application. *Int. J. Electron. Commun.* **2013**, *67*, 1030–1037. [[CrossRef](#)]
61. Ahn, H.; Baek, S.; Nam, I.; An, D.; Lee, J.K.; Jeong, M.; Kim, B.-E.; Choi, J.; Lee, O. A Fully Integrated Dual-Mode CMOS Power Amplifier with an Autotransformer-Based Parallel Combining Transformer. *IEEE Microw. Wirel. Compon. Lett.* **2017**, *27*, 833–835. [[CrossRef](#)]
62. Tsai, J.H. Design of a 5.2-GHz CMOS Power Amplifier Using TF-Based 2-Stage Dual-Radial Power Splitting/Combining Architecture. *IEEE Trans. Circuits Syst. I Regul. Pap.* **2019**, *7*, 68. [[CrossRef](#)]
63. Tsai, J.-H. Design of a 5.3-GHz 31.3-dBm Fully Integrated CMOS Power Amplifier Using Folded Splitting and Combining Architecture. *IEEE Trans. Very Large Scale Integr. Syst.* **2019**, *27*, 1527–1536. [[CrossRef](#)]
64. Choi, H.-W.; Choi, S.; Lim, J.T.; Kim, C.Y. 1-W, High-Gain, High-Efficiency, and Compact Sub-GHz Linear Power Amplifier Employing a 1:1 Transformer Balun in 180-nm CMOS. *IEEE Microw. Wirel. Compon. Lett.* **2020**, *30*, 779–781. [[CrossRef](#)]
65. Wang, T.; Qian, H.J.; Yang, B.; Luo, X. 1.2–2.8-GHz 32.4-dBm Digital Power Amplifier with Balance-Compensated Matching Network. *IEEE Microw. Wirel. Compon. Lett.* **2021**, *31*, 41–44. [[CrossRef](#)]
66. Yang, B.; Qian, H.J.; Luo, X. Quadrature Switched/Floated Capacitor Power Amplifier with Reconfigurable Self-Coupling Canceling Transformer for Deep Back-Off Efficiency Enhancement. *IEEE J. Solid-State Circuits* **2021**, *56*, 3715–3727. [[CrossRef](#)]
67. Yang, B.; Qian, H.J.; Wang, T.; Luo, X. A CMOS Wideband Watt-Level 4096-QAM Digital Power Amplifier Using Reconfigurable Power-Combining Transformer. *IEEE J. Solid-State Circuits* **2023**, *58*, 357–370. [[CrossRef](#)]
68. Doherty, W.H. A New High Efficiency Power Amplifier for Modulated Waves. *Proc. Inst. Radio Eng.* **1936**, *24*, 1163–1182. [[CrossRef](#)]
69. Vasjanov, A.; Barzdenas, V. Comparison of CMOS Power Amplifier Topologies for a Wideband Doherty Architecture. In Proceedings of the 2017 Open Conference of Electrical, Electronic and Information Sciences (eStream), Vilnius, Lithuania, 27 April 2017; pp. 1–4. [[CrossRef](#)]
70. Eswaran, U.; Ramiah, H.; Kanesan, J. Power Amplifier Design Methodologies for Next Generation Wireless Communications. *IETE Tech. Rev.* **2014**, *31*, 241–248. [[CrossRef](#)]
71. Camarchia, V.; Pirola, M.; Quaglia, R.; Jee, S.; Cho, Y.; Kim, B. The Doherty Power Amplifier: Review of Recent Solutions and Trends. *IEEE Trans. Microw. Theory Tech.* **2015**, *63*, 559–571. [[CrossRef](#)]
72. Deltimple, N.; Carneiro, M.L.; Kerhervé, E.; Carvalho, P.H.P.; Belot, D. Integrated Doherty RF CMOS Power Amplifier Design for Average Efficiency Enhancement. In Proceedings of the 2015 IEEE International Wireless Symposium (IWS 2015), Shenzhen, China, 30 March–1 April 2015; pp. 1–4. [[CrossRef](#)]

73. Hu, S.; Kousai, S.; Wang, H. A Broadband Mixed-Signal CMOS Power Amplifier with a Hybrid Class-G Doherty Efficiency Enhancement Technique. *IEEE J. Solid-State Circuits* **2016**, *51*, 598–613. [[CrossRef](#)]
74. Kaymaksut, E.; Reynaert, P. Dual-Mode CMOS Doherty LTE Power Amplifier with Symmetric Hybrid Transformer. *IEEE J. Solid-State Circuits* **2015**, *50*, 1974–1987. [[CrossRef](#)]
75. Aoki, I.; Kee, S.D.; Rutledge, D.B.; Hajimiri, A. Fully integrated CMOS power amplifier design using the distributed active-transformer architecture. *IEEE J. Solid-State Circuits* **2002**, *37*, 371–383. [[CrossRef](#)]
76. Kaymaksut, E.; Reynaert, P. Transformer-Based Uneven Doherty Power Amplifier in 90 nm CMOS for WLAN Applications. *IEEE J. Solid-State Circuits* **2012**, *47*, 1659–1671. [[CrossRef](#)]
77. Levy, C.S.; Vorapipat, V.; Buckwalter, J.F. A 14-GHz, 22-dBm Series Doherty Power Amplifier in 45-nm CMOS SOI. In Proceedings of the 2016 IEEE Compound Semiconductor Integrated Circuit Symposium (CSICS), Austin, TX, USA, 23–26 October 2016; pp. 1–4. [[CrossRef](#)]
78. Traiche, S.; Slimane, A. 3 GHz CMOS Doherty power amplifier for high efficiency. In Proceedings of the 2017 Seminar on Detection Systems Architectures and Technologies (DAT), Algiers, Algeria, 20–22 February 2017; pp. 1–4. [[CrossRef](#)]
79. Jung, H.; Zhao, J.; Wang, H. A CMOS Highly Linear Doherty Power Amplifier with Multigated Transistors. *IEEE Trans. Microw. Theory Tech.* **2019**, *67*, 1883–1891. [[CrossRef](#)]
80. Yin, Y.; Li, T.; Xiong, L.; Li, Y.; Min, H.; Yan, N.; Xu, H. A Broadband Switched-Transformer Digital Power Amplifier for Deep Back-Off Efficiency Enhancement. *IEEE J. Solid-State Circuits* **2020**, *55*, 2997–3008. [[CrossRef](#)]
81. Asbeck, P.; Popovic, Z. ET Comes of Age: Envelope Tracking for Higher-Efficiency Power Amplifiers. *IEEE Microw. Mag.* **2016**, *17*, 16–25. [[CrossRef](#)]
82. Kim, B.; Kim, J.; Kim, D.; Son, J.; Cho, Y.; Kim, J.; Park, B. Push the Envelope: Design Concepts for Envelope-Tracking Power Amplifiers. *IEEE Microw. Mag.* **2013**, *14*, 68–81. [[CrossRef](#)]
83. Ruan, X.; Wang, Y.; Jin, Q. A review of envelope tracking power supply for mobile communication systems. *CPSS Trans. Power Electron. Appl.* **2017**, *2*, 277–291. [[CrossRef](#)]
84. Ghannouchi, F.M.; Kwan, A.K.; Younes, M.; Chen, W. DSP techniques for linearity and efficiency enhancement of multi-band envelope tracking transmitters. In Proceedings of the 2014 Asia-Pacific Microwave Conference, Sendai, Japan, 4–7 November 2014; pp. 1082–1084.
85. Woo, J.; Park, S.; Kim, U.; Kwon, Y. Dynamic Stack-Controlled CMOS RF Power Amplifier for Wideband Envelope Tracking. *IEEE Trans. Microw. Theory Tech.* **2014**, *62*, 3452–3464. [[CrossRef](#)]
86. Park, B.; Kim, D.; Kim, S.; Cho, Y.; Kim, J.; Kang, D.; Jin, S.; Moon, K.; Kim, B. High-Performance CMOS Power Amplifier with Improved Envelope Tracking Supply Modulator. *IEEE Trans. Microw. Theory Tech.* **2016**, *64*, 798–809. [[CrossRef](#)]
87. Ham, J.; Bae, J.; Kim, H.; Seo, M.; Lee, H.; Hwang, K.C.; Lee, K.-Y.; Park, C.-S.; Heo, D.; Yang, Y. CMOS Power Amplifier Integrated Circuit with Dual-Mode Supply Modulator for Mobile Terminals. *IEEE Trans. Circuits Syst. I Regul. Pap.* **2016**, *63*, 157–167. [[CrossRef](#)]
88. Kahn, L.R. Single-Sideband Transmission by Envelope Elimination and Restoration. *Proc. IRE* **1952**, *40*, 803–806. [[CrossRef](#)]
89. Mamdouh, A.; Aboudina, M.; Mohieldin, A.N.; Hussien, F. CMOS A Multi-Band High-Efficiency Envelope Elimination and Restoration CMOS Power Amplifier. *Microelectron. J.* **2020**, *102*, 104823. [[CrossRef](#)]
90. Oishi, K.; Yoshida, E.; Sakai, Y.; Takauchi, H.; Kawano, Y.; Shirai, N.; Kano, H.; Kudo, M.; Murakami, T.; Tamura, T.; et al. A 1.95 GHz Fully Integrated Envelope Elimination and Restoration CMOS Power Amplifier Using Timing Alignment Technique for WCDMA and LTE. *IEEE J. Solid-State Circuits* **2014**, *49*, 2915–2924. [[CrossRef](#)]
91. Yuan, W.; Walling, J.S. A switched-capacitor controlled digital-current modulated class-E EER transmitter. In Proceedings of the 2015 IEEE 13th International New Circuits and Systems Conference (NEWCAS), Grenoble, France, 7–10 June 2015; pp. 1–4. [[CrossRef](#)]
92. Liu, X.; Zhang, H.; Mok, P.K.T.; Loung, H.C. A Multi-Loop-Controlled AC-Coupling Supply Modulator with a Mode-Switching CMOS PA in an EER System with Envelope Shaping. *IEEE J. Solid-State Circuits* **2019**, *54*, 1553–1563. [[CrossRef](#)]
93. Lee, O.; Han, J.; An, K.H.; Lee, D.H.; Lee, K.S.; Hong, S.; Lee, C.H. A Charging Acceleration Technique for Highly Efficient Cascode Class-E CMOS Power Amplifiers. *IEEE J. Solid-State Circuits* **2010**, *45*, 2184–2197. [[CrossRef](#)]
94. Raab, F. Efficiency of Outphasing RF Power-Amplifier Systems. *IEEE Trans. Commun.* **1985**, *33*, 1094–1099. [[CrossRef](#)]
95. Hung, T.P.; Choi, D.K.; Larson, L.E.; Asbeck, P.M. CMOS Outphasing Class-D Amplifier with Chireix Combiner. *IEEE Microw. Wirel. Compon. Lett.* **2007**, *17*, 619–621. [[CrossRef](#)]
96. Xu, H.; Palaskas, Y.; Ravi, A.; Sajadieh, M.; Elmala, M.; Soumyanath, K. A 28.1 dBm class-D outphasing power amplifier in 45nm LP digital CMOS. In Proceedings of the 2009 Symposium on VLSI Circuits, Kyoto, Japan, 16–18 June 2009; pp. 206–207.
97. Ding, L.; Hur, J.; Banerjee, A.; Hezar, R.; Haroun, B. A 25 dBm Outphasing Power Amplifier with Cross-Bridge Combiners. *IEEE J. Solid-State Circuits* **2015**, *50*, 1107–1116. [[CrossRef](#)]
98. Beltran, R.; Raab, F.H.; Velazquez, A. HF outphasing transmitter using class-E power amplifiers. In Proceedings of the 2009 IEEE MTT-S International Microwave Symposium Digest, Boston, MA, USA, 7–12 June 2009; pp. 757–760. [[CrossRef](#)]
99. Hu, Z.; de Vreede, L.C.N.; Alavi, M.S.; Calvillo-Cortes, D.A.; Staszewski, R.B.; He, S. A 5.9 GHz RFDAC-based outphasing power amplifier in 40-nm CMOS with 49.2% efficiency and 22.2 dBm power. In Proceedings of the 2016 IEEE Radio Frequency Integrated Circuits Symposium (RFIC), San Francisco, CA, USA, 22–24 May 2016; pp. 206–209. [[CrossRef](#)]

100. Martelius, M.; Stadius, K.; Lemberg, J.; Nieminen, T.; Roverato, E.; Kosunen, M.; Ryyänen, J.; Anttila, L.; Valkama, M. Class D CMOS power amplifier with on/off logic for a multilevel outphasing transmitter. In Proceedings of the 2016 IEEE International Symposium on Circuits and Systems (ISCAS), Montreal, QC, Canada, 22–25 May 2016; pp. 710–713. [\[CrossRef\]](#)
101. Banerjee, A.; Hezar, R.; Ding, L.; Haroun, B. A 29.5 dBm Class-E Outphasing RF Power Amplifier with Efficiency and Output Power Enhancement Circuits in 45 nm CMOS. *IEEE Trans. Circuits Syst. I* **2017**, *64*, 1977–1988. [\[CrossRef\]](#)
102. Ghahremani, A.; Annema, A.; Nauta, B. Outphasing Class-E Power Amplifiers: From Theory to Back-Off Efficiency Improvement. *IEEE J. Solid-State Circuits* **2018**, *53*, 1374–1386. [\[CrossRef\]](#)
103. Martelius, M.; Stadius, K.; Lemberg, J.; Roverato, E.; Nieminen, T.; Antonov, Y.; Anttila, L.; Valkama, M.; Kosunen, M.; Ryyänen, J. A Class-D Tri-Phasing CMOS Power Amplifier with an Extended Marchand-Balun Power Combiner. *IEEE Trans. Microw. Theory Tech.* **2020**, *68*, 1022–1034. [\[CrossRef\]](#)
104. Banerjee, A.; Ding, L.; Hezar, R. A High Efficiency Multi-Mode Outphasing RF Power Amplifier with 31.6 dBm Peak Output Power in 45nm CMOS. *IEEE Trans. Circuits Syst. I Regul. Pap.* **2020**, *67*, 815–828. [\[CrossRef\]](#)
105. Kang, S.; Choi, B.; Kim, B. Linearity analysis of CMOS for RF application. *IEEE Trans. Microw. Theory Tech.* **2003**, *51*, 972–977. [\[CrossRef\]](#)
106. Golar, S.; Moloudi, S.; Abidi, A.A. Processes of AM-PM Distortion in Large-Signal Single-FET Amplifiers. *IEEE Trans. Circuits Syst. I Regul. Pap.* **2017**, *64*, 245–260. [\[CrossRef\]](#)
107. Xi, T.; Huang, S.; Guo, S.; Gui, P.; Huang, D.; Chakraborty, S. High-Efficiency E-Band Power Amplifiers and Transmitter Using Gate Capacitance Linearization in a 65-nm CMOS Process. *IEEE Trans. Circuits Syst. II Express Briefs* **2017**, *64*, 234–238. [\[CrossRef\]](#)
108. Wang, C.; Vaidyanathan, M.; Larson, L.E. A capacitance-compensation technique for improved linearity in CMOS class-AB power amplifiers. *IEEE J. Solid-State Circuits* **2004**, *39*, 1927–1937. [\[CrossRef\]](#)
109. Camarchia, V.; Colantonio, P.; Giannini, F.; Giofrè, R.; Jiang, T.; Pirola, M.; Quaglia, R.; Ramella, C. A Design Strategy for AM/PM Compensation in GaN Doherty Power Amplifiers. *IEEE Access* **2017**, *5*, 22244–22251. [\[CrossRef\]](#)
110. Cho, M. Analog Predistortion for Improvement of Rf Power Amplifier Efficiency and Linearity. Ph.D. Thesis, Georgia Institute of Technology, Atlanta, GA, USA, 2016.
111. Li, F. Linearization of Power Amplifiers in Wide Band Communication Systems by Digital Baseband Predistortion Technique. Ph.D. Thesis, Universite De Nantes, Nantes, France, 2012.
112. Borel, A.; Barzdėnas, V. A Review of the Basic Power Amplifier Linearization Methods. In Proceedings of the 2020 IEEE Open Conference of Electrical, Electronic and Information Sciences (eStream), Vilnius, Lithuania, 30 April 2020; pp. 1–4. [\[CrossRef\]](#)
113. Dawson, J.L.; Lee, T.H. Cartesian feedback for RF power amplifier linearization. In Proceedings of the 2004 American Control Conference, Boston, MA, USA, 30 June–2 July 2004; Volume 1, pp. 361–366. [\[CrossRef\]](#)
114. Monticelli, D. System approaches to power management. In Proceedings of the APEC Seventeenth Annual IEEE Applied Power Electronics Conference and Exposition (Cat. No.02CH37335), Dallas, TX, USA, 10–14 March 2002; Volume 1, pp. 3–7. [\[CrossRef\]](#)
115. Tee, L.; Sacchi, E.; Bockock, R.; Wongkomet, N.; Gray, P. A Cartesian-Feedback Linearized CMOS RF Transmitter for EDGE Modulation. In Proceedings of the 2006 Symposium on VLSI Circuits, 2006, Digest of Technical Papers, Honolulu, HI, USA, 15–17 June 2006; pp. 232–233. [\[CrossRef\]](#)
116. Atress, A.B.; Raafat, H.; Shawkey, H.; Zaki, A. Zigbee Power Amplifier Linearization Using Cartesian Feedback. *Int. J. Adv. Res.* **2016**, *4*, 1769–1776.
117. Sowlati, T.; Rozenblit, D.; Pullela, R.; Damgaard, M.; McCarthy, E.; Koh, D.; Ripley, D.; Balteanu, F.; Gheorghe, I. Quad-band GSM/GPRS/EDGE polar loop transmitter. *IEEE J. Solid-State Circuits* **2004**, *39*, 2179–2189. [\[CrossRef\]](#)
118. Nakatani, T.; Kimball, D.; Larson, L.; Asbeck, P. 0.7–1.8 GHz multiband digital polar transmitter using watt-class current-mode class-D CMOS power amplifier and digital envelope modulation technique for reduced spurious emissions. *Int. J. Microwave Wireless Technol.* **2013**, *5*, 271–284. [\[CrossRef\]](#)
119. Zheng, S.; Luong, H.C. A CMOS WCDMA/WLAN Digital Polar Transmitter with AM Replica Feedback Linearization. *IEEE J. Solid-State Circuits* **2013**, *48*, 1701–1709. [\[CrossRef\]](#)
120. Liao, H.; Chen, J.; Chiou, H.; Chen, C. High-linearity CMOS feedforward power amplifier for WiMAX application. In Proceedings of the 2008 Asia-Pacific Microwave Conference, Hong Kong, China, 16–20 December 2008; pp. 1–4. [\[CrossRef\]](#)
121. Chen, Y.-H.; Kao, K.; Chao, C.-Y.; Lin, K. A 24 GHz CMOS power amplifier with successive IM2 feed-forward IMD3 cancellation. In Proceedings of the 2015 IEEE MTT-S International Microwave Symposium, Phoenix, AZ, USA, 17–22 May 2015; pp. 1–4. [\[CrossRef\]](#)
122. Garcia, P.; de Mingo, J.; Valdovinos, A.; Ortega, A. An adaptive digital method of imbalances cancellation in LINC transmitters. *IEEE Trans. Veh. Technol.* **2005**, *54*, 879–888. [\[CrossRef\]](#)
123. Lee, H.; Lee, H.; Paek, J.; Hong, S. A CMOS power amplifier for Multi-mode LINC architecture. In Proceedings of the 2010 IEEE Radio and Wireless Symposium (RWS), New Orleans, LA, USA, 10–14 January 2010; pp. 41–44. [\[CrossRef\]](#)
124. Lee, H.; Jang, S.; Hong, S. A Hybrid Polar-LINC CMOS Power Amplifier with Transmission Line Transformer Combiner. *IEEE Trans. Microwave Theory Tech.* **2013**, *61*, 1261–1271. [\[CrossRef\]](#)
125. Yao, J.; Long, S.I. Power Amplifier Selection for LINC Applications. *IEEE Trans. Circuits Syst. II Express Briefs* **2006**, *53*, 763–767. [\[CrossRef\]](#)
126. Katz, A.; Wood, J.; Chokola, D. The Evolution of PA Linearization: From Classic Feedforward and Feedback Through Analog and Digital Predistortion. *IEEE Microw. Mag.* **2016**, *17*, 32–40. [\[CrossRef\]](#)

127. Rey, C.G. Predistorter linearizes CDMA power amplifiers. *Microwaves RF Mag.* **1998**, *44*, 114–123.
128. Yi, J.; Yang, Y.; Park, M.; Kang, W.; Kim, B. Analog predistortion linearizer for high-power RF amplifiers. *IEEE Trans. Microw. Theory Tech.* **2000**, *48*, 2709–2713. [[CrossRef](#)]
129. Son, K.Y.; Koo, B.; Hong, S. A CMOS Power Amplifier with a Built-In RF Predistorter for Handset Applications. *IEEE Trans. Microwave Theory Tech.* **2012**, *60*, 2571–2580. [[CrossRef](#)]
130. Paramesh, J.; Bishop, R.; Soumyanath, K.; Allstot, D.J. A four-antenna receiver in 90-nm CMOS for beamforming and spatial diversity. *IEEE J. Solid-State Circuits* **2005**, *40*, 2515–2524. [[CrossRef](#)]
131. Afsahi, A.; Rael, J.J.; Behzad, A.; Chien, H.M.; Pan, M.; Au, S.; Ojo, A.; Lee, C.P.; Anand, S.B.; Chien, K.; et al. A Low-Power Single-Weight-Combiner 802.11abg SoC in 0.13  $\mu\text{m}$  CMOS for Embedded Applications Utilizing An Area and Power Efficient Cartesian Phase Shifter and Mixer Circuit. *IEEE J. Solid-State Circuits* **2008**, *43*, 1101–1118. [[CrossRef](#)]
132. Rostomyan, N.; Jayamon, J.A.; Asbeck, P.M. 15 GHz Doherty Power Amplifier with RF Predistortion Linearizer in CMOS SOI. *IEEE Trans. Microw. Theory Techn.* **2018**, *66*, 1339–1348. [[CrossRef](#)]
133. Mariappan, S.; Rajendran, J.; Ramiah, H.; Mak, P.-I.; Yin, J.; Martins, R.P. An 800 MHz-to-3.3 GHz 20-MHz Channel Bandwidth WPD CMOS Power Amplifier For Multiband Uplink Radio Transceivers. *IEEE Trans. Circuits Syst. II Exp. Briefs* **2021**, *68*, 1178–1182. [[CrossRef](#)]
134. Mariappan, S.; Rajendran, J.; Yusof, Y.M.; Noh, N.M.; Yarman, B.S. An 0.4–2.8 GHz CMOS Power Amplifier with On-Chip Broadband-Pre-Distorter (BPD) Achieving 36.1–38.6% PAE and 21 dBm Maximum Linear Output Power. *IEEE Access* **2021**, *9*, 48831–48840. [[CrossRef](#)]
135. Mariappan, S.; Rajendran, J.; Chen, Y.; Mak, P.-I.; Martins, R.P. A 1.7-to-2.7GHz 35–38% PAE Multiband CMOS Power Amplifier Employing a Digitally-Assisted Analog Pre-Distorter (DAAPD) Reconfigurable Linearization Technique. *IEEE Trans. Circuits Syst. II Exp. Briefs* **2021**, *68*, 3381–3385. [[CrossRef](#)]
136. Mariappan, S.; Rajendran, J.; Kumar, N.; Othman, M.; Nathan, A.; Grebennikov, A.; Yarman, B.S. A Wide-Bandwidth PVT-Reconfigurable CMOS Power Amplifier with an Integrated Tunable-Output Impedance Matching Network. *Micromachines* **2023**, *14*, 530. [[CrossRef](#)]
137. Tsai, J.-H. A 5.3-GHz 30.1-dBm Fully Integrated CMOS Power Amplifier with High-Power Built-In Linearizer. *IEEE Microw. Wirel. Technol. Lett.* **2023**, *33*, 431–434. [[CrossRef](#)]
138. Woo, W.; Kenney, J.S. A predistortion linearization system for high power amplifiers with low-frequency envelope memory effects. In Proceedings of the IEEE MTT-S International Microwave Symposium Digest, Long Beach, CA, USA, 17 June 2005; p. 4. [[CrossRef](#)]
139. Paaso, H.; Mammela, A. Comparison of direct learning and indirect learning predistortion architectures. In Proceedings of the 2008 IEEE International Symposium on Wireless Communication Systems, Reykjavik, Iceland, 21–24 October 2008; pp. 309–313. [[CrossRef](#)]
140. Zhou, D.; DeBrunner, V. A novel adaptive nonlinear predistorter based on the direct learning algorithm. In Proceedings of the 2004 IEEE International Conference on Communications (IEEE Cat. No. 04CH37577), Paris, France, 20–24 June 2004; Volume 4, pp. 2362–2366. [[CrossRef](#)]
141. Li, Y.; Zhang, X. Adaptive digital predistortion based on MC-FQD-RLS algorithm using indirect learning architecture. In Proceedings of the 2010 2nd International Conference on Advanced Computer Control, Shenyang, China, 27–29 March 2010; pp. 240–242. [[CrossRef](#)]
142. Cho, Y.; Lee, J.; Jin, S.; Park, B.; Moon, J.; Kim, J.; Kim, B. Fully Integrated CMOS Saturated Power Amplifier with Simple Digital Predistortion. *IEEE Microw. Wirel. Compon. Lett.* **2014**, *24*, 533–535. [[CrossRef](#)]
143. Wong, A.; Godoy, P.; Carnu, O.; Li, H.; Zhao, X.; Olyaei, A.; Ghaffari, A.; Tam, S.-W.; Winoto, R.; Tsang, R. A dual-core power combining digital power amplifier for 802.11 b/g/n with +26.8 dBm linear output power in 28 nm CMOS. In Proceedings of the 2017 IEEE Radio Frequency Integrated Circuits Symposium (RFIC), Honolulu, HI, USA, 4–6 June 2017; pp. 192–195. [[CrossRef](#)]
144. Kim, W.; Yang, K.S.; Han, J.; Chang, J.J.; Lee, C.H. An EDGE/GSM Quad-Band CMOS Power Amplifier. *IEEE J. Solid-State Circuits* **2014**, *49*, 2141–2149. [[CrossRef](#)]
145. Kim, H.; Bae, J.; Ham, J.; Gu, J.; Seo, M.; Hwang, K.; Lee, K.-Y.; Park, C.-S.; Yang, Y. Efficiency enhanced CMOS digitally controlled dynamic bias switching power amplifier for LTE. *Microw. Opt. Technol. Lett.* **2015**, *57*, 2315–2321. [[CrossRef](#)]
146. Kim, B.; Lee, D.-H.; Hong, S.; Park, M. A Multi-Band CMOS Power Amplifier Using Reconfigurable Adaptive Power Cell Technique. *IEEE Microw. Wireless Compon. Lett.* **2016**, *26*, 616–618. [[CrossRef](#)]
147. Ren, J.; Dai, R.; He, J.; Zhang, Z.; Zou, S. A high power CMOS cascode power amplifier with adaptive dynamic bias control for linearity enhancement. *Microw. Opt. Technol. Lett.* **2020**, *62*, 2451–2457. [[CrossRef](#)]
148. Mariappan, S.; Rajendran, J.; Noh, N.; Yusof, Y.; Kumar, N. A 23.3 dBm CMOS power amplifier with third-order gm cancellation linearization technique achieving OIP3 of 34 dBm. *Circuit World* **2021**, *48*, 215–222. [[CrossRef](#)]
149. Rawat, A.S.; Rajendran, J.; Mariappan, S.; Shasidharan, P.; Kumar, N.; Yarman, B.S. A 919 MHz–923 MHz, 21 dBm CMOS Power Amplifier with Bias Modulation Linearization Technique Achieving PAE of 29% for LoRa Application. *IEEE Access* **2022**, *10*, 79365–79378. [[CrossRef](#)]
150. Rawat, A.S.; Rajendran, J.; Mariappan, S.; Kumar, N.; Mak, P.-I.; Martins, R.P. A 27-dBm, 0.92-GHz CMOS Power Amplifier with Mode Switching and a High-Q Compact Inductor (HQCI) Achieving a 30% Back-Off PAE. *IEEE Trans. Circuits Syst. II* **2023**, *70*, 121–125. [[CrossRef](#)]

151. Kang, S.; Sung, E.; Hong, S. Dynamic Feedback Linearizer of RF CMOS Power Amplifier. *IEEE Microw. Wireless Compon. Lett.* **2018**, *28*, 915–917. [[CrossRef](#)]
152. Eriksson, K.; Darwazeh, I.; Zirath, H. InP DHBT Distributed Amplifiers with Up to 235-GHz Bandwidth. *IEEE Trans. Microw. Theory Tech.* **2015**, *63*, 1334–1341. [[CrossRef](#)]
153. Krishnamurthy, K. Ultra-Broadband, Efficient, Microwave Power Amplifiers in Gallium Nitride HEMT Technology. Ph.D. Thesis, University of California, Santa Barbara, CA, USA, 2000.
154. Hsiao, C.; Su, T.; Hsu, S.S.H. CMOS Distributed Amplifiers Using Gate–Drain Transformer Feedback Technique. *IEEE Trans. Microw. Theory Tech.* **2013**, *61*, 2901–2910. [[CrossRef](#)]
155. Chen, P.-H.; Yeh, K.-S.; Kao, J.-C.; Wang, H. A high-performance DC–80 GHz distributed amplifier in 40-nm CMOS digital process. In Proceedings of the 2014 IEEE MTT-S International Microwave Symposium (IMS2014), Tampa, FL, USA, 1–6 June 2014; pp. 1–3. [[CrossRef](#)]
156. Zhang, Y.; Ma, K. A 2–22 GHz CMOS Distributed Power Amplifier with Combined Artificial Transmission Lines. *IEEE Microw. Wireless Compon. Lett.* **2017**, *27*, 1122–1124. [[CrossRef](#)]
157. Tarar, M.M.; Negra, R. Design and Implementation of Wideband Stacked Distributed Power Amplifier in 0.13  $\mu\text{m}$  CMOS Using Uniform Distributed Topology. *IEEE Trans. Microw. Theory Tech.* **2017**, *65*, 5212–5222. [[CrossRef](#)]
158. Sira, D.; Larsen, T. Process, Voltage and Temperature Compensation Technique for Cascode Modulated PAs. *IEEE Trans. Circuits Syst. I* **2013**, *60*, 2511–2520. [[CrossRef](#)]
159. Krishnanji, S. Design of a Variable Gain Amplifier for an Ultra Wideband Receiver. Master’s Thesis, Texas A&M University, College Station, TX, USA, 2005.
160. Albasha, L.; Loo, C.; Nguyen, D.; Doherty, G.; El-Gamal, M.N. An Ultra-Wideband Digitally Programmable Power Amplifier with Efficiency Enhancement for Cellular and Emerging Wireless Communication Standards. *IEEE Trans. Circuits Syst. I* **2016**, *63*, 1579–1591. [[CrossRef](#)]
161. Leuschner, S.; Mueller, J.; Klar, H. A 1.8GHz wide-band stacked-cascode CMOS power amplifier for WCDMA applications in 65nm standard CMOS. In Proceedings of the 2011 IEEE Radio Frequency Integrated Circuits Symposium, Baltimore, MD, USA, 5–7 June 2011; pp. 1–4. [[CrossRef](#)]
162. Jeon, H.; Ryu, M.J.; Kim, B.; Kim, D. A Cascode Feedback Bias Technique for Linear CMOS Power Amplifiers in a Multistage Cascode Topology. *IEEE Trans. Microw. Theory Tech.* **2013**, *61*, 890–901. [[CrossRef](#)]
163. Wu, H.; Cheng, Q.; Li, X.; Fu, H. Analysis and Design of an Ultrabroadband Stacked Power Amplifier in CMOS Technology. *IEEE Trans. Circuits Syst. II* **2016**, *63*, 49–53. [[CrossRef](#)]
164. Kang, S.; Jeong, G.; Hong, S. Study on Dynamic Body Bias Controls of RF CMOS Cascode Power Amplifier. *IEEE Microw. Wireless Compon. Lett.* **2018**, *28*, 705–707. [[CrossRef](#)]
165. Guo, T.; Lu, Z.; Tang, K.; Yang, C.; Yu, B.; Zheng, Y. A Floating-Body Transistor-Based Power Amplifier for Sub-6-GHz 5G Applications in SOI CMOS 130-nm Process. *IEEE Trans. Circuits Syst. II* **2022**, *69*, 4088–4092. [[CrossRef](#)]
166. Jose, S.; Lee, H.-J.; Ha, D.; Choi, S.S. A low-power CMOS power amplifier for ultra wideband (UWB) applications. In Proceedings of the 2005 IEEE International Symposium on Circuits and Systems, Kobe, Japan, 23–26 May 2005; Volume 5, pp. 5111–5114. [[CrossRef](#)]
167. Murad, S.A.Z.; Pokharel, R.K.; Sapawi, R.; Kanaya, H.; Yoshida, K. High efficiency, good linearity, and excellent phase linearity of 3.1–4.8 GHz CMOS UWB PA with a current-reused technique. *IEEE Trans. Consumer Electron.* **2010**, *56*, 1241–1246. [[CrossRef](#)]
168. Murad, S.A.Z.; Pokharel, R.K.; Galal, A.I.A.; Sapawi, R.; Kanaya, H.; Yoshida, K. An Excellent Gain Flatness 3.0–7.0 GHz CMOS PA for UWB Applications. *IEEE Microw. Wirel. Compon. Lett.* **2010**, *20*, 510–512. [[CrossRef](#)]
169. Ginzberg, N.; Cohen, E. A Wideband CMOS Power Amplifier with 52% Peak PAE Employing Resistive Shunt Feedback for Sub-6 GHz 5G Applications. *IEEE Microw. Wirel. Technol. Lett.* **2023**, *33*, 192–195. [[CrossRef](#)]
170. Peng, X.-Q.; Yu, W.-H.; Mak, P.-I.; Martins, R.P. A 26.3 dBm 2.5 to 6 GHz wideband class-D switched-capacitor power amplifier with 40% peak PAE. In Proceedings of the 2014 IEEE International Conference on Electron Devices and Solid-State Circuits, Chengdu, China, 1–2 June 2014; pp. 1–2. [[CrossRef](#)]
171. Aparin, V.; Dunworth, J.; Seward, L.; Yuan, W.; Walling, J.S. A transformer combined quadrature switched capacitor power amplifier in 65nm CMOS. In Proceedings of the 2016 14th IEEE International New Circuits and Systems Conference (NEWCAS), Vancouver, BC, Canada, 26–29 June 2016; pp. 1–4. [[CrossRef](#)]
172. Yuan, W.; Aparin, V.; Dunworth, J.; Seward, L.; Walling, J.S. A quadrature switched capacitor power amplifier in 65nm CMOS. In Proceedings of the 2015 IEEE Radio Frequency Integrated Circuits Symposium (RFIC), Phoenix, AZ, USA, 17–19 May 2015; pp. 135–138. [[CrossRef](#)]
173. Yuan, W.; Walling, J.S. A multiphase switched capacitor power amplifier in 130nm CMOS. In Proceedings of the 2016 IEEE Radio Frequency Integrated Circuits Symposium (RFIC), San Francisco, CA, USA, 22–24 May 2016; pp. 210–213. [[CrossRef](#)]
174. Cho, H.; Lee, M.; Park, C.; Park, J.Y. A Fully Integrated Switched Capacitor using Low Temperature and Wet Release Process for Reconfigurable CMOS Triple-band Power Amplifier. In Proceedings of the 2019 IEEE Asia-Pacific Microwave Conference (APMC), Singapore, 10–13 December 2019; pp. 1467–1469. [[CrossRef](#)]
175. Bai, Z.; Yuan, W.; Azam, A.; Walling, J.S. A split-array, C-2C switched-capacitor power amplifier in 65 nm CMOS. In Proceedings of the 2017 IEEE Radio Frequency Integrated Circuits Symposium (RFIC), Honolulu, HI, USA, 4–6 June 2017; pp. 336–339. [[CrossRef](#)]

176. Huang, C.; Chen, Y.; Zhang, T.; Sathe, V.; Rudell, J.C. A 40 nm CMOS single-ended switch-capacitor harmonic-rejection power amplifier for ZigBee applications. In Proceedings of the 2016 IEEE Radio Frequency Integrated Circuits Symposium (RFIC), San Francisco, CA, USA, 22–24 May 2016; pp. 214–217. [[CrossRef](#)]
177. Yoo, S.; Walling, J.S.; Woo, E.; Allstot, D.J. A power-combined switched-capacitor power amplifier in 90nm CMOS. In Proceedings of the 2011 IEEE Radio Frequency Integrated Circuits Symposium (RFIC), Baltimore, MD, USA, 5–7 June 2011; pp. 1–4. [[CrossRef](#)]
178. Yoo, S.; Hung, S.; Yoo, S. A Watt-Level Quadrature Class-G Switched-Capacitor Power Amplifier with Linearization Techniques. *IEEE J. Solid-State Circuits* **2019**, *54*, 1274–1287. [[CrossRef](#)]
179. Ginzberg, N.; Cohen, E. Switched-Capacitor RF Power Amplifiers: A Review of Efficiency and Linearity Considerations. In Proceedings of the 2018 IEEE International Conference on the Science of Electrical Engineering in Israel (ICSEE), Eilat, Israel, 21–23 November 2018; pp. 1–5. [[CrossRef](#)]
180. Truppi, A.; Samori, C.; Lacaita, A.L.; Levantino, S.; Ronchi, M.; Sosio, M. Impact of CMOS Scaling on Switched-Capacitor Power Amplifiers. In Proceedings of the 2018 IEEE International Symposium on Circuits and Systems (ISCAS), Florence, Italy, 27–30 May 2018; pp. 1–4. [[CrossRef](#)]
181. Goswami, S.; Kim, H.; Dawson, J.L. A Frequency-Agile RF Frontend Architecture for Multi-Band TDD Applications. *IEEE J. Solid-State Circuits* **2014**, *49*, 2127–2140. [[CrossRef](#)]
182. Yoo, S.; Walling, J.S.; Woo, E.C.; Allstot, D.J. A switched-capacitor power amplifier for EER/polar transmitters. In Proceedings of the 2011 IEEE International Solid-State Circuits Conference, San Francisco, CA, USA, 20–24 February 2011; pp. 428–430. [[CrossRef](#)]
183. Yuan, W.; Aparin, V.; Dunworth, J.; Seward, L.; Walling, J.S. A Quadrature Switched Capacitor Power Amplifier. *IEEE J. Solid-State Circuits* **2016**, *51*, 1200–1209. [[CrossRef](#)]
184. Bai, Z.; Azam, A.; Johnson, D.; Yuan, W.; Walling, J.S. Split-Array, C-2C Switched-Capacitor Power Amplifiers. *IEEE J. Solid-State Circuits* **2018**, *53*, 1666–1677. [[CrossRef](#)]
185. Jin, H.; Kim, D.; Kim, B. 9.5 efficient digital quadrature transmitter based on IQ cell sharing. In Proceedings of the 2015 IEEE International Solid-State Circuits Conference-(ISSCC) Digest of Technical Papers, San Francisco, CA, USA, 22–26 February 2015; pp. 1–3. [[CrossRef](#)]
186. Singh, S.P.; Prabhakar, A.; Bhattacharyya, A.B. C-2C ladder voltage dividers for application in all-MOS A/D convertors. *Electron. Lett.* **1982**, *18*, 537–538. [[CrossRef](#)]
187. Lee, S.W.; Chung, H.J.; Han, C.H. C-2C digital-to-analogue converter on insulator. *Electron. Lett.* **1999**, *35*, 1242–1243. [[CrossRef](#)]
188. Xiong, W.; Guo, Y.; Zschieschang, U.; Klauk, H.; Murmann, B. A 3-V, 6-Bit C-2C Digital-to-Analog Converter Using Complementary Organic Thin-Film Transistors on Glass. *IEEE J. Solid-State Circuits* **2010**, *45*, 1380–1388. [[CrossRef](#)]
189. Bai, Z.; Azam, A.; Walling, J.S. A Frequency Tuneable Switched-Capacitor PA in 65nm CMOS. In Proceedings of the 2019 IEEE Radio Frequency Integrated Circuits Symposium (RFIC), Boston, MA, USA, 2–4 June 2019; pp. 295–298. [[CrossRef](#)]
190. Raja, I.; Banerjee, G. A 0.75–2.5-GHz All-Digital RF Transmitter with Integrated Class-E Power Amplifier for Spectrum Sharing Applications in 5G Radios. *IEEE Trans. VLSI Syst.* **2020**, *28*, 2109–2121. [[CrossRef](#)]

**Disclaimer/Publisher’s Note:** The statements, opinions and data contained in all publications are solely those of the individual author(s) and contributor(s) and not of MDPI and/or the editor(s). MDPI and/or the editor(s) disclaim responsibility for any injury to people or property resulting from any ideas, methods, instructions or products referred to in the content.